2020-12-13

Improving the physical basis for updraft dynamics in deep convection parameterizations

Peters, J.M.; Morrison, H.; Zhang, G.J.; Powell, S.W.

AGU

Peters, J. M., H. Morrison, G. J. Zhang, and S. W. Powell. "Improving the physical basis for updraft dynamics in deep convection parameterizations." Journal of Advances in Modeling Earth Systems: e2020MS002282.
http://hdl.handle.net/10945/66477

Improving the physical basis for updraft dynamics in deep convection parameterizations

J. M. Peters[1], H. Morrison[2], G. J. Zhang[3], and S. W. Powell[1]

[1]Naval Postgraduate School, Monterey, CA
[2]National Center for Atmospheric Research, Boulder, CO
[3]Scripps Institution of Oceanography, University of California, San Diego, La Jolla, California

Key Points:

- Improved dynamical assumptions in cumulus parameterization
- Incorporating vertical wind shear into cumulus parameterization
- Analytic equations for vertical mass flux and vertical velocity

Corresponding author: John M. Peters, jmpeters@nps.edu

This article has been accepted for publication and undergone full peer review but has not been through the copyediting, typesetting, pagination and proofreading process, which may lead to differences between this version and the Version of Record. Please cite this article as doi: 10.1029/2020MS002282.

Abstract

This article presents a new deep convective parameterization that determines cloud characteristics based on a specified cloud size distribution. The vertical profiles of cloud properties are determined by analytic equations, which formulate entrainment with an inverse relationship to cloud width. In line with recent studies of large eddy simulations, cloud widths are assumed to be constant with height and vertical mass flux (M) characteristics of the clouds are therefore regulated by the vertical velocity profile. The parameterization is configured to work with existing cloud base M closure formulations, with the closure predicting the total cloud area rather than the cloud base M directly. Analytic formulae are also used to connect the vertical wind shear magnitude to the cloud size distribution, wherein larger shear magnitudes result in more numerous large updrafts than weaker shear magnitudes, which is in line with recent research results. The parameterization is compared against 10 deep convective large eddy simulations with varying thermodynamic and vertical wind shear profiles. Results show dramatic improvements in the prediction of normalized M, detrainment, and the properties of detrained air over the existing Zhang and McFarlane (1995) scheme. In particular, the new model is able to correctly portray the transition from a bottom-heavy M profile in weakly sheared environments, to a top-heavy M profile in strongly sheared environments.

Plain Language Summary

This article presents a new avenue for representing thunderstorms in climate and global forecast models. The model assumes that cloud widths follow an exponential distribution, with many narrow clouds and few wide clouds. The properties of cloud cores are represented by analytic equations, which saves computational expense. Entrainment is assumed to be inversely proportional to clouds' widths, which is consistent with known cloud behavior. The effects of vertical wind shear on the cloud size distribution are included. Cloud properties and behavior in the new parameterization agree well with high resolution simulations of deep convection.

1 Introduction

Plume models are the centerpiece for most modern cumulus parameterizations of deep convection (CPs, e.g., all of those based on Arakawa & Schubert, 1974), and therefore encapsulate the effects of entrainment and detrainment on clouds in CPs. These simple models are meant to represent the properties of shallow and deep convective cores in a physically reasonable and computationally efficient manner. Typically either a single plume, or a small number of plumes, are used in CPs to represent the aggregate effect of many cumulus updrafts within a given global climate model (GCM) grid cell.

Without question, the largest outstanding problem in the formulation of plume models is how to represent the mixing of cloudy air with surrounding environmental air through entrainment and detrainment (e.g., De Rooy et al., 2013; Hirota et al., 2014). Entrainment typically dilutes cloud core properties, contributing decreases in both cloud moist static energy and buoyancy with height (e.g., Hannah, 2017). Entrainment also adds mass to the cloud envelope, leading to an increase in M with height. In contrast, detrainment typically "concentrates" cloud core properties, contributing increases in both cloud moist static energy and buoyancy with height (e.g., Hannah, 2017). Detrainment also removes mass from the cloud envelope, leading to a decrease in M with height. Entrainment and detrainment together strongly regulate cloud depth, mass flux, and consequently cloud feedbacks with the large scale environment (Arakawa & Schubert, 1974). Thus, an accurate representation of these processes in a plume model is essential to building a reliable CP. Despite the importance of these processes, there is little consensus on how a cloud's properties and environment regulate entrainment and detrainment.

Most plume models for deep moist convection in CPs emulate canonical laboratory studies and dimensional analyses of dry convection in fluids from the middle 20th century (e.g., Squires & Turner, 1962). In these studies, a point source of positive buoyancy incites a steady column of rising fluid that entrains surrounding fluid parcels as it rises, thereby predictably increasing its M with height. The plume models' reliance on these early fluid studies of dry convection may contribute to difficulties in accurately representing convective entrainment in CPs. For instance, the plume M equation is often approximated as[1]:

$$\frac{1}{M}\frac{dM}{dz} = \varepsilon - \delta, \tag{1}$$

where ε and δ are fractional entrainment and detrainment length scales respectively, and the sum of $\varepsilon - \delta$ is often positive. It is immediately apparent that when $\varepsilon - \delta$ is positive, M will increase monotonically and exponentially with height. Obviously detrainment must occur at some level in the atmosphere since real updrafts do not extend upward indefinitely; in CPs, it is often assumed that detrainment simply happens instantaneously at the level of neutral buoyancy (e.g., Arakawa & Schubert, 1974; Zhang & McFarlane, 1995). This behavior is relatively consistent with the dry convective plumes that underpin the older fluid studies, which gradually expand and increase their mass flux with height. In contrast, the profile of M in numerous large eddy simulations (LES) of deep moist convection has been shown to peak in the middle troposphere, and decrease upward from this level for both ensembles of clouds (e.g., Khairoutdinov et al., 2009; Sherwood et al., 2013; Romps & Charn, 2015) and within individual clouds (e.g., Peters, Hannah, & Morrison, 2019). Furthermore, detrainment happens over a substantial portion of clouds' depth (e.g., Romps, 2010; Dawe & Austin, 2011; Hernandez-Deckers & Sherwood, 2018; Peters, Morrison, Hannah, et al., 2020), bearing little resemblance to the delta-function representing detrainment in CPs. This formulation in eq. 1 is therefore an outright problem, since this equation behaves in a way that is fundamentally different than that of real deep moist convection. There are many remedies for this problem in past literature that are too numerous for us to comprehensively summarize here. We instead focus on three examples that are most relevant to the present work.

In the Zhang and McFarlane (1995) scheme (hereafter the ZM scheme), many plumes are used instead of just one plume. Each of these plumes has a different ε and level of neutral buoyancy (LNB). Though each individual plume obeys eq. 1 with all detrainment occurring immediately at the plume's LNB, net detrainment from the entire cloud ensemble will occur over a wide vertical range because of the variations in the plume termination heights. Furthermore, if one considers the total ensemble M (rather than that of individual plumes), a maximum will occur in the middle troposphere with progressively decreasing M above. In these ways, the ZM scheme more accurately represents the characteristics of convection than schemes using a single plume.

However, there remain unphysical attributes of this scheme's behavior. For instance, it is always assumed that at least one plume is undiluted. Yet, air in cloud cores is often substantially diluted by the time it surpasses the lowest few km of the troposphere (Romps & Kuang, 2010), aside from the rare cases of supercell thunderstorms (Peters, Nowotarski, & Morrison, 2019; Peters, Nowotarski, & Mullendore, 2020; Peters, Nowotarski, & Mulholland, 2020). Furthermore, all plumes are assumed to have the same cloud base mass flux in the ZM scheme. In accordance with eq. 1, the plumes with the largest entrainment rates and the lowest termination heights will have the largest M above cloud base. Since a large entrainment corresponds to a small cloud radius (e.g., Morrison, 2017; Lecoanet & Jeevanjee, 2018; Hernandez-Deckers & Sherwood, 2018; Morrison et al., 2020),

[1] M is defined here with units of kg s^{-1}, which allows us to consider the updraft size distribution in terms of physical distance (rather than fractional distance). Some studies alternatively define M per unit area with units of kg s^{-1} m^{-2}. Dividing our M by the domain area A gives the mass flux per unit area.

this implies that the narrowest clouds comprise the largest percentage of the M in the cloud ensemble. However, large eddy simulations show just the opposite - that the widest and deepest clouds comprise the largest percentage of M (e.g., Hernandez-Deckers & Sherwood, 2016; Peters, Hannah, & Morrison, 2019). Thus, the configuration of plumes in the ZM scheme remains at odds with the behavior of real clouds, biasing processes toward shallow and narrow clouds and away from deeper and wider clouds. This unphysical behavior is partially remedied in the upper troposphere because the plumes with large entrainment rates terminate at lower altitudes than those with small entrainment rates, and thus the least diluted plumes begin to dominate the scheme's portrayal of cloud properties aloft.

The Romps (2016) scheme (hereafter the R scheme) escapes the usage of eq. 1 altogether. In this scheme, parcels are assumed to undergo a distribution of entrainment rates as they rise, resulting in a range of parcel purities at any given height, and a corresponding distribution of M among this range of purities. This scheme also relies on the vertical velocity (w) equation, forcing air to detrain during the portion of its ascent between its LNB and termination height (as determined by the level at which $w = 0$ m s^{-1}). This formulation produces much more realistic profiles of M and entrainment because its treatment of the aforementioned processes relies on behaviors that are physically consistent with moist convection in LES. It is worth noting, however, that the R scheme suffers from the same unphysical behavior as the ZM scheme, in that the largest M will become biased toward the portion of the distribution that has experienced the greatest entrainment-driven dilution. This is, again, inconsistent with LES of deep convection where the largest clouds accomplish the most M.

The so-called ED(MF)$^{\mathrm{n}}$ approach (where EDMF stands for "eddy diffusivity mass flux," and the n exponent indicates the usage of multiple plumes) of Neggers (2015) for parameterizing shallow convection has taken a much different approach than typical deep convective schemes. In the ED(MF)$^{\mathrm{n}}$ approach, there is an assumed initial distribution of plume widths. Narrower plumes are assumed to entrain more and reach lower termination heights than wider plumes. Like in the ZM scheme, this range of plume characteristics gives rise to a more realistically distributed region of convective detrainment. Another noteworthy aspect of this approach is that model closure evolves from the determination of a bulk cloud base M to the determination of the cloud size distribution — and the later property of the cloud population is something that is more readily verified with observations. In addition to the ED(MF)$^{\mathrm{n}}$ framework, several past schemes have also used an initial assumed distribution of cloud radii to determine the characteristics of their cloud ensemble (e.g., Donner, 1993; Wagner & Graf, 2010).

We believe that the approach taken in the ED(MF)$^{\mathrm{n}}$ scheme may unilaterally remedy the aforementioned unphysical behaviors in other deep convective schemes. Accordingly, we have developed a new parameterization for deep convection — termed the multiplume analytic model (MAP) — that more closely follows the ED(MF)$^{\mathrm{n}}$ approach than that of traditional deep convective schemes. Like in the ED(MF)$^{\mathrm{n}}$ scheme, the basis for our model is an ensemble of clouds with a specific initial size distribution. Fractional entrainment rates are formulated in our model based on analytic expressions derived in Morrison (2017) and Peters, Nowotarski, and Mullendore (2020), and are inversely proportional to cloud radius, which follows previous schemes that have formulated entrainment inversely with cloud width (e.g., Donner, 1993; Wagner & Graf, 2010; Neggers, 2015). This follows past research that has emphasized the relationship between cloud radius and entrainment, wherein narrow clouds tend to have larger fractional entrainment rates than wider clouds (e.g., Kyle et al., 1976; Tian & Kuang, 2016; Morrison, 2017; Hannah, 2017; Hernandez-Deckers & Sherwood, 2018; Peters, Nowotarski, & Morrison, 2019; Peters, Nowotarski, & Mullendore, 2020). Consistent with recent large eddy simulations and theoretical studies (e.g., Hernandez-Deckers & Sherwood, 2016, 2018), we assume constant updraft radii

with height. We also use a simple analytic w equation (rather than equation 1) to determine the M profiles of individual plumes.

Finally, the most novel aspect of the MAP is the inclusion of dependencies of updraft mass flux on deep layer vertical wind shear. None of the existing CPs have included the dynamic influence of vertical wind shear on cloud characteristics. These dependencies of deep convection on shear have been characterized in several of our recent studies, which generally show that as deep layer vertical wind shear increases updrafts become wider (e.g., Peters, Nowotarski, & Morrison, 2019; Peters, Nowotarski, & Mullendore, 2020; Peters, Nowotarski, & Mulholland, 2020; Peters, Morrison, Nowotarski, et al., 2020). We validate our model by its ability to reproduce the cloud characteristics from LES that are most relevant to CPs. The organization of this paper is as follows: Section 2 outlines the formulation of our model, section 3 compares the behavior of our model to LES, and section 4 summarizes our conclusions and discusses implications of the results.

2 MAP formulation

2.1 Cloud variables that interact with the large scale environment

Since our model will be evaluated in its ability to predict the variables that are most relevant to CPs, we review the budgets for these relevant variables as they were outlined in Arakawa and Schubert (1974). The time tendency of the horizontal average (denoted by an overbar) across a GCM grid cell of an arbitrary scalar Λ is:

$$\rho \frac{\partial \overline{\Lambda}}{\partial t}_{c} = \rho \frac{\partial}{\partial t} \left[(1-\xi)\, \widetilde{\Lambda} + \xi \Lambda \right], \tag{2}$$

where $\xi \equiv \frac{a_c}{A}$, a_c is the horizontal cloud area at a given height, A is the total area of a GCM grid cell, $\widetilde{\Lambda}$ represents the horizontal average over the regions in between clouds at a given level, and Λ represents values horizontally averaged within clouds. If we assume a steady cloud population such that $\frac{\partial \Lambda}{\partial t} = \frac{\partial a_c}{\partial t} = 0$, we may use eqs. 16 and 17 from Arakawa and Schubert (1974) in combination with our eq. 2 to write:

$$\widetilde{\Lambda} = (1-\xi)^{-1} \left(\overline{\Lambda} - \xi \Lambda \right) \tag{3}$$

$$\rho \frac{\partial \overline{\Lambda}}{\partial t}_{c} = \underset{\text{a)}}{\frac{D}{A} \left(\Lambda_D - \widetilde{\Lambda} \right)} + \underset{\text{c)}}{\frac{M_c}{A} \frac{\partial \widetilde{\Lambda}}{\partial z}} + \underset{\text{d)}}{\frac{\xi}{A\,(1-\xi)} \frac{\partial}{\partial z} \left[\overline{M} \left(\overline{\Lambda} - \Lambda \right) \right]}, \tag{4}$$

$$\rho \frac{\partial \overline{s}}{\partial t}_{c} = \underset{\text{a)}}{\frac{D}{A} \left(s_D - \widetilde{s} \right)} - \underset{\text{b)}}{\frac{D}{A} L_H q_{t,D}} \underset{\text{c)}}{\frac{M_c}{A} \frac{\partial \widetilde{s}}{\partial z}} + \underset{\text{d)}}{\frac{\xi}{A\,(1-\xi)} \frac{\partial}{\partial z} \left[\overline{M} \left(\overline{s} - s \right) \right]} \tag{5}$$

$$\rho \frac{\partial \overline{q_v}}{\partial t}_{c} = \underset{\text{a)}}{\frac{D}{A} \left(q_{v,D} - \widetilde{q_v} \right)} - \underset{\text{b)}}{\frac{D}{A} q_{t,D}} + \underset{\text{c)}}{\frac{M_c}{A} \frac{\partial \widetilde{q_v}}{\partial z}} + \underset{\text{d)}}{\frac{\xi}{A\,(1-\xi)} \frac{\partial}{\partial z} \left[\overline{M} \left(\overline{q_v} - q_v \right) \right]}, \tag{6}$$

where $s \equiv c_p T + gz$ is dry static energy, q_v is water vapor mixing ratio, q_t is the mixing ratio of total condensed water, D is the net detrainment rate of the cumulus cloud population, s_D, $q_{v,D}$, $q_{t,D}$, and Λ_D are the properties of detrained s, q_v, q_t, and other arbitrary scalars Λ respectively, L_H is latent heat from condensation, freezing, and sublimation, M_c is the M of the cloud population, ρ is density, and the subscript c on the time tendency denotes that we are only considering contributions from cloud processes. Note that eq. 4 applies to all arbitrary scalars aside from s and q_v, whereas eq. 3 is valid for s and q_v in addition to all other arbitrary scalars.

The physical processes related to individual terms are:

a. detrainment of cloud properties into the surrounding large scale environment,
b. evaporation of detrained cloud water into the surrounding large scale environment,
c. vertical advection between clouds driven by convection.
d. vertical flux of perturbation cloud properties.

The variables that must be provided by a CP are therefore D, s_D, $q_{v,D}$, $q_{t,D}$, M_c, a_c, s, and q_v. In subsequent sub-sections, we outline our model formulations for each of these quantities.

It was assumed in Arakawa and Schubert (1974) that $\xi << 1$, and thus $\widetilde{s} \approx \overline{s}$ and $\widetilde{q_v} \approx \overline{q_v}$. This assumption has become problematic for modern GCMs and global forecast models due to increasing model resolution and a commensurate decrease in the effective grid spacing (e.g., Arakawa et al., 2011; Arakawa & Jung, 2011; Arakawa & Wu, 2013; Grell & Freitas, 2014; Han et al., 2017). Here, we relax this assumption since a_c is obtainable from our cloud size distribution. However, we have implicitly retained the assumption in Arakawa and Schubert (1974) that $\overline{\nabla \cdot (\mathbf{V}\Lambda)} \approx \nabla \cdot \left(\bar{\mathbf{V}}\bar{\Lambda}\right)$, where $\mathbf{V}$ is the horizontal wind. Scale aware formulations for this horizontal advection term are possible within our CP framework, but are left to future work.

2.2 Cloud size distribution

To prescribe a size distribution for our cloud ensemble, we first define a function $N(R)$ which represents the number of updrafts with radii of less than radius R that exit the boundary layer and seed the cumulus population. In principle, $N(R)$ is a free parameter that we could set to any distribution; however, our intent is to choose a distribution that mimics the cloud width distribution in LES, along with observations of tropical cumulonimbus (e.g., Fig 3 in LeMone & Zipser, 1980). From our analyses of LES later in this study, we have chosen an exponential distribution which features a large number of small updrafts and a small number of large updrafts; however, there is certainly room for future consideration and/or modification of this distribution. The characteristics of our exponential distribution are modulated by a maximum updraft size R_m, a slope factor χ, and an amplitude N_0 such that:

$$\frac{dN}{dR} = N_0 e^{-\chi \frac{R}{R_m}}. \tag{7}$$

using eq. 7, the cloud area a_c may be written as:

$$a_c = \pi \int_{R_0}^{R_m} N_0 e^{-\chi \frac{R}{R_m}} R^2 dR = \pi N_0 \left[\frac{R_m e^{-\chi \frac{R_0}{R_m}}}{\chi^3} \left(2R_m^2 + 2R_m R_0 \chi + \chi^2 R_0^2\right) - \frac{R_m^3 e^{-\chi}}{\chi^3} \left(2 + 2\chi + \chi^2\right) \right], \tag{8}$$

where R_0 is a lower bound for the updraft R distribution that will be discussed later.

The structure of weakly sheared deep convective updrafts is decidedly unsteady, and is often characterized by a chain of rising semi-discrete moist thermals (e.g., Sherwood et al., 2013; Romps & Charn, 2015; Morrison et al., 2020; Peters, Morrison, Hannah, et al., 2020). This behavior in LES may seem at odds with our assumption of a steady cloud population. However, we reconcile this apparent disparity by assuming that updraft characteristics are steady when averaged over the period of time of a GCM grid time step, and horizontally averaging over many clouds within a given R.

2.3 Total ensemble M

Next we define the M characteristics of the cloud ensemble. We begin by considering the M of the jth cloud type $m_j = \pi R_j^2 \rho_j w_j$. Cloud type j have radii R_j that fall within the range R and $R + \Delta R$, where ΔR is a small radius increment. We also define the ensemble M function $M = M(R, z)$ which represents the total ensemble M for

all updrafts with radii less than R. Since LES shows that R is fairly constant with height for moist thermals in weakly sheared deep convection (e.g., Hernandez-Deckers & Sherwood, 2016, 2018) and comparatively steady updrafts that occur in strongly sheared environments (e.g., Peters, Nowotarski, & Morrison, 2019; Peters, Nowotarski, & Mullendore, 2020), we assume that vertical variations in m_j occur exclusively from vertical variations in w_j and hold R constant with height for a given cloud type. The total M for all j type clouds is:

$$M(R+\Delta R,z) - M(R,z) = \sum m_j = \pi\rho R_j^2 w_j \left[N(R+\Delta R,z) - N(R,z)\right], \tag{9}$$

Taking the limit as $\Delta R \to 0$ and combining the result with eq. 7 gives:

$$dM = \pi\rho R^2 w N_0 e^{-\chi\frac{R}{R_m}} dR. \tag{10}$$

Now we must express w as a function of R and z. To accomplish this, we begin by following the methodology of Morrison (2017) to derive expressions for the properties at the center of a rising moist thermal. In that study, horizontal mixing was parameterized using an eddy diffusivity approach to arrive at the following expression for a passive tracer C (eq. 9 in that study):

$$\frac{dC}{dz} = -\varepsilon\left(C - \overline{C}\right) = -\frac{2k^2 L}{P_r R^2}\left(C - \overline{C}\right) \tag{11}$$

where k is a mixing constant, L is a mixing length, P_r is the turbulent Prandtl number, $\overline{C}$ is the large scale tracer concentration, and the fractional entrainment rate is $\varepsilon \equiv \frac{2k^2}{P_r R}$. Conceptually, the mixing length L should scale proportionally to R, and we set $L = R$ hereafter for simplicity (as was done in Peters, Morrison, Nowotarski, et al., 2020). Though this expression was originally intended to represent properties at the center of a rising moist thermal, we assume that the expression also applies to horizontally and temporally averaged updraft core properties in our cloud ensemble. In fact, it can be shown that eq. 11 also applies for a steady-state plume by simply replacing $\frac{d}{dz}$ (i.e., the vertical derivative following a thermal along the thermal's path of ascent) with $\frac{\partial}{\partial z}$ (i.e., the local vertical derivative) in the in-line equation above eq. 8 in Morrison (2017) and proceeding with subsequent steps in the derivation, which yield an identical result to eq. 11 here.

A few assumptions that are baked into this equation warrant discussion here. First, it was assumed that the mixing of environmental properties into an updraft core is primarily accomplished by turbulent mixing, whereas organized inflow (i.e., dynamic entrainment) draws air into the cloud without directly diluting the updraft core (see Morrison, 2017; Morrison et al., 2020, for a detailed discussion of this assumption). Second, this expression does not contain a detrainment term, which may seem at odds with our desire to provide a more accurate representation of detrainment relative to previous updraft core models. However, it can be shown that if we assume that the properties of detrained air are the same as the updraft core C, then the detrainment term vanishes from the equation. For instance, a $\delta\left(C - C_D\right)$ would appear in eq. 11, where C_D is the tracer concentration of detrained air and δ is the fractional detrainment rate. However, here we assume $C_D = C$ so that this detrainment term vanishes. So eq. 11 does not expressly neglect detrainment, and remains consistent with the foundational assumptions of our model.

With eq. 11 at hand, Morrison (2017) assumed a constant saturation with respect to water, neglected ice processes, neglected condensate loading, and used the mixing formulation in eq. 11 to represent the influences of lateral mixing of moisture and temperature on updraft buoyancy B. He obtained the following expression for buoyancy B:

$$B(z,R) = B_{AD}(z) + R^{-1}\Omega_1(z) + R^{-1}\Omega_2(z)B(z,R), \tag{12}$$

where $\Omega_1 = -\frac{2H_v g k^2}{c_p P_r}\int_{z^*=0}^{z^*=z} \frac{q_{s,0}(1-\overline{RH})}{\overline{T_v}\left(1+\frac{H_v^2 \overline{q_s}}{c_p R_v \overline{T_v}^2}\right)} dz^*$, $\Omega_2 = \frac{-k^2 z}{P_r}$, B_{AD} is the buoyancy for a moist adiabatically lifted air parcel computed relative to the large scale environment, H_v is the latent heat of vaporization, g is the gravitational constant, c_p is the specific heat of air at constant pressure, $\overline{q_s}$ is the saturation mixing ratio of the large scale environment, R_v is the specific gas constant for water vapor, $\overline{T_v}$ is the virtual temperature of the large scale environment, and $\overline{RH}$ is the relative humidity of the large scale environment. The 2nd term on the right-hand side of eq. 12 represents the effects of dry air entrainment on condensation rates and evaporation within the updraft, and the 3rd term on the right-hand side represents the direct dilution of updraft B by the entrainment of environmental air. For simplicity of notation in subsequent analysis, we define $z = 0$ at the level of free convection (LFC). Eq. 12 has been shown to accurately portray B in simulated updrafts (e.g., Peters, Nowotarski, & Morrison, 2019; Peters, Morrison, Nowotarski, et al., 2020), despite the absence of ice or precipitation loading in this formula. This consistent accuracy may stem from compensating biases between the two omissions, whereby omitting ice results in a low bias in B diagnosis, but omitting hydrometeor loading contributes a compensatory high bias.

Using the definitions $w_B(z,R)^2 \equiv 2\int_{z^*=0}^{z^*=z} B(z,R)dz^*$, $CAPE(z) \equiv \int_{z^*=0}^{z^*=z} B_{AD}(z)dz^*$, $K(z) \equiv \frac{1}{z}\int_{z^*=0}^{z^*=z} \Omega_1(z)dz^*$, and $\lambda \equiv -\frac{\Omega_2}{3z}$, Peters, Morrison, Nowotarski, et al. (2020) obtained the following expression from eq. 12:

$$w_B^2 = w_b^2 + \frac{2CAPE - \frac{2z}{R}K}{1+\frac{z\lambda}{R}}, \tag{13}$$

where the subscript B indicates that this is an approximation for w that only takes into account buoyant accelerations and w_b is w at the LFC (i.e., cloud base). For the simplest implementation of our model here, we will neglect the influence of dynamic pressure accelerations on w. This is justified by previous studies that have shown that dynamic pressure acceleration minimally alters the maximum value of w achieved within the core of thermals (e.g., Peters, 2016; Morrison & Peters, 2018; Peters, Nowotarski, & Morrison, 2019; Peters, Morrison, Nowotarski, et al., 2020). We further assume that buoyancy pressure acceleration reduces upward buoyancy acceleration by a factor of $\left(1+\frac{H^2}{2\alpha^2 R^2}\right)^{-1}$ (e.g., Morrison, 2016), giving:

$$w^2 = \left(1+\frac{H^2}{2\alpha^2 R^2}\right)^{-1} w_B^2, \tag{14}$$

where α is a constant parameter typically set to 0.8 (e.g., Morrison & Peters, 2018) and H is the depth of $B > 0$ m s^{-2}. Combining eq. 14, eq. 13, eq. 10, and integrating over a range of R gives our total ensemble M:

$$M_c = M(R_m, z) = \pi N_0 \int_{R=R_0(z)}^{R=R_m} \rho R^2 \sqrt{\left(1+\frac{H^2}{2\alpha^2 R^2}\right)^{-1}\left(w_b^2 + \frac{2CAPE - \frac{2z}{R}K}{1+\frac{z\lambda}{R}}\right)} e^{-\chi\frac{R}{R_m}} dR. \tag{15}$$

At this point we add several constraints to prevent unphysical behavior. First, dM is set to zero for negative w_B, meaning that we are disallowing M to exist when w becomes negative. Because of this constraint, we must set the lower bound of our integral R_0 to correspond to the minimum R value at a given height that yields an updraft with $w \geq 0$ m s^{-1}. From setting w_B^2 to zero in eq. 13, we obtain:

$$R_0(z) = \frac{2zK - 2z\lambda w_b^2}{w_b^2 + 2CAPE}, \tag{16}$$

where we set $R_0(z) = R_m$ when eq. 16 yields a negative value, or when $R_0(z) > R_m$.

2.4 Detrainment and the properties of detrained air

For a parameterization to drive large scale variable tendencies realistically, the mass exchange between the cloud free atmosphere and cloudy updrafts must be accurately characterized through total ensemble detrainment D (i.e., see eqs. 5 and 6). The equation relating the total M $M(R_m, z)$ of our ensemble to entrainment E and D is:

$$\frac{dM(R_m, z)}{dz} = E - D, \tag{17}$$

where E and D have units of kg s^{-1} m^{-1} (not to be confused with fractional entrainment and detrainment which have units of inverse length). We cannot simply take entrainment to be positive values of $\frac{dM}{dz}$ and detrainment to be negative values of $\frac{dM}{dz}$ because, at any given height, both entrainment and detrainment might be occurring. This can be physically understood by considering that narrow updrafts may reach their LNB at relatively low altitudes, whereas wide updrafts may reach their LNB at comparatively high heights. Thus, narrow updrafts may primarily detrain mass at a height where a comparatively wide updraft is primarily entraining mass.

To obtain our expressions for E and D, we first write eq. 15 in a more compact form as:

$$M(R_m, z) = \int_{R=R_0(z)}^{R=R_m} dM(R, z). \tag{18}$$

Taking $\frac{d}{dz}$ of eq. 15 and applying the Liebniz integral rule gives:

$$\frac{dM(R_m, z)}{dz} = \int_{R=R_0(z)}^{R=R_m} \frac{\partial}{\partial z} dM(R, z) - dM(R_0, z)\frac{dR_0}{dz}. \tag{19}$$

We note that by definition $dM(R_0, z) = 0$ and thus $dM(R_0, z)\frac{dR_0}{dz} = 0$. We may therefore re-write eq. 15 and subsequently define E and D as:

$$\frac{dM(R_m, z)}{dz} = \underbrace{\int_{R=R_0(z)}^{R=R_m} H\left[\frac{\partial}{\partial z} dM(R, z)\right]}_{\text{total entrainment, } E} - \underbrace{\int_{R=R_0(z)}^{R=R_m} H\left[-\frac{\partial}{\partial z} dM(R, z)\right]}_{\text{total detrainment, } D}, \tag{20}$$

where H is the Heaviside step function. This definition of D is modeled after that of Romps (2016), wherein detrainment was assumed to occur within individual updraft elements if they are negatively buoyant and if w decreases with height.

We adopt the methodology of the ZM scheme to compute s_D and $q_{v,D}$. This scheme makes use of the quantity $h^* \equiv \overline{s} + \overline{q_s}$, where $\overline{q_s}$ is the saturation water vapor mixing ratio of the background environment. They further assumed that $h_D = h^*$. The physical reasoning for this assumption is that detrained air should leave at a height of neutral B, and thus $s_D = \overline{s}$. Detrained air should also be saturated because of its cloudy origins, and hence the assumption that $q_D = \overline{q_{v,s}}$.

2.5 Cloud microphysics

For the proof-of-concept demonstrations in this paper, we adopt the simple microphysical parameterization of Zhang and McFarlane (1995) with modifications to account for ice. The budget for q_t is written as:

$$\frac{\partial q_t}{\partial z} = -\left(\frac{2k^2}{P_r R} + c\right) q_t - \frac{\partial q_s}{\partial z}, \tag{21}$$

where c is the precipitation rate, $-\frac{\partial q_s}{\partial z}$ is a condensation rate, and $\frac{2k^2}{P_r R}$ is the turbulent fractional entrainment rate used to compute B, assuming there is no condensed water

in the environment surrounding a cloud. The particular solution to eq. 21 with $q_t = 0$ kg kg^{-1} at the LFC is:

$$q_t(R,z) = -e^{-\frac{2k^2}{P_r R}z - \int_{z^*=0}^{z^*=z} c dz^*} \int_{z^*=0}^{z^*=z} e^{\frac{2k^2}{P_r R}z + \int_{z^*=0}^{z^*=z} c dz^*} \frac{\partial q_s}{\partial z^*} dz^*. \tag{22}$$

To obtain q_l (cloud liquid mixing ratio) and q_i (cloud ice mixing ratio) from $q_t = q_l + q_i$, we adopt the simple piecewise linear function F of Romps (2016), whereby all cloud liquid water is assumed to freeze between temperatures of 273.15 and 240 K, such that the proportionality of q_l and q_i transitions linearly from all q_l at 273.15 K, to all q_i at 240 K. Thus, $q_l = Fq_t$, $q_i = (1-F)q_t$, and $F = 1$ for $T > 273.15$ K, $F = \frac{-33.15}{T-240}$ for $240 < T \leq 273.15$ K, and $F = 0$ for $T < 240$ K. For simplicity, we assume that precipitation falls at a rate of $c = c_0 F$, where $c_0 = 4^{-3}$ m^{-1} is a constant that was set to yield reasonable correspondence between the MAP and LES q_t profiles.

The profile of T for a given cloud size is obtained by first solving for B in eq. 12:

$$B = \frac{B_{AD} + \frac{\Omega_1}{R}}{1 - \frac{\Omega_2}{R}}. \tag{23}$$

Next, we approximate $B \approx g\frac{T-\overline{T}}{\overline{T}}$, and make use of the Clausius Clapeyron equation $\frac{d\ln\mu_s}{dT} = \frac{L_v}{R_v T^2}$ wherein the temperature dependency of L_v is neglected and μ_s is the saturation vapor pressure, to obtain:

$$T = \overline{T}\left(\frac{B}{g} + 1\right), \tag{24}$$

$$q_s = \frac{\epsilon \mu_{tr}}{\overline{p}} e^{-\frac{L_v}{R_v}\left(\frac{1}{T} - \frac{1}{T_{tr}}\right)}, \tag{25}$$

where μ_{tr} is a reference saturation vapor pressure at the triple point temperature T_{tr} and $\overline{p}$ is the background environmental pressure.

Values of detrained cloud liquid $q_{l,D}$ and ice $q_{i,D}$ are obtained by assuming that the mixing ratios of detrained liquid and ice are equal to the M weighted values in the cloud at a given height, such that:

$$q_{l,D}(z) = \left(\int_{R=R_0(z)}^{R=R_m} dMdR\right)^{-1} \int_{R=R_0}^{R=R_m} q_l dMdR, \tag{26}$$

$$q_{i,D}(z) = \left(\int_{R=R_0(z)}^{R=R_m} dMdR\right)^{-1} \int_{R=R_0}^{R=R_m} q_i dMdR. \tag{27}$$

Thus, $DL_t q_{t,D} = D\left(L_v q_{v,D} + L_i q_{i,D}\right)$, where L_v and L_i are the latent heats of condensation and fusion respectively. All detrained condensate is either assumed to serve as a cloud source in the parent GCM when clouds are already present, or immediately evaporates/sublimates when clouds are not already present, as is the case in the ZM scheme. While the microphysics outlined in this section are rudimentary, the MAP could conceivably be used with a more sophisticated microphysics scheme which would make use of the cloud variables outlined thus far.

2.6 Closure

The implementation of traditional CPs requires the determination of the cloud base M M_b, which itself modulates the magnitude of the total M accomplished by the cloud population. In these traditional models, M profiles are normalized by M_b such that M_b appears as an independent parameter in the cloud M equations. In contrast, M_b does

not appear explicitly within our equations. This means that if we trusted that our initial updraft size distribution were quantitatively realistic, we could circumvent the need to specify M_b completely because we have already obtained a quantitative expression for $M(R_m, z)$ at each level. This strategy is used for determining the shallow cumulus ensemble M in the ED(MF)$^{\mathrm{n}}$ method of Neggers (2015), which relies upon cloud size distributions gleaned from observations and LES (e.g., Neggers et al., 2019) for closure rather than M_b.

However, M_b also plays an important role in CPs by modulating the cloud-driven variable tendencies in the planetary boundary layer (PBL). There are explicit assumptions about the structure of updrafts in the PBL in the ED(MF)$^{\mathrm{n}}$ approach which allows this approach to completely circumvent reliance on M_b. In contrast, we have not made any explicit assumptions about the extension of deep convective updrafts into the PBL here, and we therefore cannot characterize PBL tendencies from deep convection without some treatment of M_b in our model framework. We have refrained from a detailed analysis of updrafts in the PBL because the structure of such updrafts is likely to be strongly dependent on a range of processes, such as dry convection in the PBL, cold pools, synoptic scale forcing for ascent, dynamics within the lower parts of existing updrafts, and terrain features to name a few. It is possible that such a framework for extending updraft properties into the PBL could be developed in the future through an analysis of dynamic and buoyant pressure accelerations below cloud base (e.g., Brown & Nowotarski, 2018) and along the edge of cold pools (e.g., Bryan & Rotunno, 2014; Jeevanjee & Romps, 2015); however, we leave such analysis to future work.

Instead, we devise a relatively simple procedure to marry our model with existing closure schemes. The premise of this procedure is that M_b from existing closure should regulate the total number of updrafts, but not the "slope" of the cloud size distribution χ. Thus, variations in M_b will alter the magnitude, but not change the shape of the vertical profile of $M(R_m, z)$. M_b should therefore dictate N_0 but not χ. To connect these variables, we evaluate eq. 15 at $z = 0$ giving:

$$M_b = \frac{2}{3}\pi N_0 \int_{R=R_0(z)}^{R=R_m} \rho R^2 w_b e^{-\chi \frac{R}{R_m}} dR. \tag{28}$$

Assuming w_b is identical for all cloud sizes and $R_0(0) = 0$, we may analytically evaluate the integral in eq. 28 and solve for N_0 giving:

$$N_0 = \frac{3\chi^3 M_b}{2\pi\rho w_b R_m^3 \left[2 - e^{-\chi}\left(\chi^2 + 2\chi + 2\right)\right]}. \tag{29}$$

We must then set w_b to something reasonable, say, a few m s^{-1}. Based on an analysis of horizontally averaged updraft w at the LFC in our simulations (not shown), we expect w_b to range from 1-5 m s^{-1} with some dependence on the magnitude of the vertical wind shear. A thorough examination of how this quantity should be determined, however, is left to future work. Given our assumptions, N_0 depends on M_b only and a standard closure procedure can be used to simply solve for N_0 as the remaining unknown in our system of equations rather than M_b.

As a final step, we must determine R_m which modulates the slope of the updraft distribution. For instance, a situation with large R_m will shift part of the M toward large updrafts and alter the shape of the distribution of $M(R_m, z)$ relative to a situation where R_m is small. In LES of weakly sheared tropical environments, maximum updraft R are typically 1-2 km (e.g., Hernandez-Deckers & Sherwood, 2016). At present, there is not a clear understanding of why this length scale is preferred, but it seems sensible to set our lower bound on R_m to 1.5 km for the proof-of-concept tests in this paper. For the full implementation of this scheme into weather and climate models, a better approach may be to scale R_m with the depth of the PBL; however, more analysis of this potential relationship would be needed before putting this idea into practice.

In environments with moderate-to-strong vertical wind shear shear, there is growing evidence that the magnitude of this shear strongly regulates the width of the widest updrafts (Warren et al., 2017; Peters, Nowotarski, & Morrison, 2019; Peters, Nowotarski, & Mullendore, 2020; Peters, Nowotarski, & Mulholland, 2020; Peters, Morrison, Nowotarski, et al., 2020). An avenue for predicting R_m in the presence of shear was presented in Peters, Morrison, Nowotarski, et al. (2020). That study focused on supercell thunderstorms and developed an analytic expression for supercell updraft maximum w, w_{max}. However, the aforementioned study also evaluated the performance of the analytic expression with simulations of nonsupercell deep convection, and found that the expression accurately predicted w_{max} for the most intense updrafts in those simulations as well. Assuming that the widest updrafts contained the largest w_{max}, we may envision the expression from this study as a predictor for w_{max} within the widest updraft in a given cloud environment.

A key element of the derivation in Peters, Morrison, Nowotarski, et al. (2020) was the connection drawn between the vertical wind shear and updraft width. Hereafter, we assume that updrafts are cylindrical, and that all of the low-level cloud-relative flow with nonzero CAPE that encounters the cross-sectional area of the cylindrical updraft will enter the updraft and turn upward. This assumption may seem restrictive; however, recent modeling studies have supported the idea that most of the air encountering the lower part of deep convective updrafts does indeed enter and ascend (e.g., Peters, Nowotarski, & Morrison, 2019; Peters, Morrison, Nowotarski, et al., 2020). The cylindrical continuity equation for a Boussinesq atmosphere is:

$$\frac{1}{r}\frac{\partial ru}{\partial z} + \frac{\partial w}{\partial z} = 0, \tag{30}$$

where u and w are radially averaged. Area integrating from the updraft center to the radius R where radially averaged w vanishes, and vertically integrating from the surface to the height L of w_{max} gives:

$$u_{in} = \frac{R\alpha w_{max}}{2L}, \tag{31}$$

where $u_{in} \equiv \frac{1}{L}\int_{z=0}^{z=L} u dz$ is the average flow across the updraft periphery below L and α is once again defined such that $\alpha w_{max} = \frac{1}{R}\int_{r=0}^{r=R} wRdr$. The cloud relative flow is defined as $\mathbf{V}_{cr} \equiv \mathbf{V} - \mathbf{V}_c$, where $\mathbf{V}$ is the horizontal wind in the GCM grid cell, and $\mathbf{V}_c$ is the horizontal cloud motion. It was shown in (e.g., Peters, Morrison, Nowotarski, et al., 2020) that $|\mathbf{V}_{cr}| \approx \frac{V_{BWD}}{2}$ is a reasonable approximation, where V_{BWD} is the effective bulk wind difference[2] (EBWD) magnitude from the background environment. Because the cloud-relative flow approaches a cylinder with a curved surface, one must divide the cloud relative flow by a factor of π (see eq. 16 in Peters, Morrison, Nowotarski, et al., 2020) when substituting into eq. 31, which gives

$$R_m = L\frac{2V_{BWD}}{\pi\alpha w_{max}}, \tag{32}$$

(see the discussion regarding eq. 17 in Peters, Morrison, Nowotarski, et al., 2020, for more details). The parameter L is difficult to obtain independently of other parameters, so we approximate L as the depth of positive B_{AD} to avoid cumbersome iterative methods for solving for R_m. In combining eq. 32 with eq. 13, where $CAPE$ and K in eq. 13 are evaluated at the LNB for an adiabatically lifted air parcel, w_{max} is obtained from the following equation (e.g., eq. 18 and 19 in Peters, Morrison, Nowotarski, et al., 2020):

$$w_{max}^3 + \frac{V_{BWD}}{\lambda\pi\alpha}w_{max}^2 + \frac{2K}{\lambda}w_{max} - \frac{2V_{BWD}}{\lambda\pi\alpha}CAPE = 0. \tag{33}$$

[2] The EBWD is defined in Thompson et al. (2007) as the magnitude of the wind vector at an altitude half way through the region of positive B_{AD} in a sounding, minus the wind vector at the lowest point with convective available potential energy greater than 100 J kg^{-1} and convective inhibition less than -250 J kg^{-1}.

Thus, in the simple proof-of-concept analysis here, if solutions to eqs. 32 and 33 for R_m yield values greater than 1.5 km, we use these solutions for R_m. Otherwise, we set R_m to the minimum value of 1.5 km. A similar approach may be adopted for full implementation of the scheme, whereby R_m is set to the maximum of either the PBL depth (as in Wagner & Graf, 2010) or the value obtained as the solution to eqs. 32 and 33. Additional work is needed to more comprehensively determine the environmental factors that determine R_m when vertical shear is weak; however, as will be shown in forthcoming sections, our current treatment of this parameter results in a close match between the MAP and the properties of deep convection in LES.

2.7 Model implementation

The MAP must first be provided with a vertical profile of atmospheric state variables. For the simple exercises later in this paper, this initial profile is simply the sounding that was used to initialize the LESs. If the scheme were to be implemented in a CP, the parent weather or climate model would provide such a profile at each grid cell, and the scheme would be executed if the appropriate conditions in a convective trigger function were met.

The first calculations to be performed are the determinations of $CAPE$ and K, which require one and two vertical integration steps respectively. For simplicity here, we will simply lift an air parcel from the first level of maximum h in the lower troposphere, although there are an array of alternative choices for the initial parcel characteristics. In the second step, we use $CAPE$ and K to determine R_m and R_0. The former involves a single evaluation of the cubic root equation and a few algebraic calculations; the latter simply involves the solution to an algebraic equation at each height and a few logical operations.

Next, we calculate dM, which is an analytical function and does not require any integration. In fact, a particular advantage of our formulation is that h need not be computed for each updraft — rather, we rely upon an analytic formula for B. Thus, the vertical integrations that are typically required to compute h, along with the iterative solutions that are needed to obtain B from h, are not required here and substantially save computation time. To obtain $M(R_m, z)$ from dM, a numerical integration is executed at each vertical level over the range R_0 to R_m. Likewise, D is computed from dM by integrating over only the ranges for which $\frac{\partial}{\partial z} dM < 0$. We obtain $q_{v,D}$ using $q_{v,D} = L_v^{-1}\left(h^* - \overline{s}\right)$ following Zhang and McFarlane (1995). Finally, updraft temperature is computed from the analytic expression for B. From updraft temperature, and using the background environmental pressure, all microphysical variables and their respective detrainment values are computed.

We have not discussed the computation of vertical fluxes of other variables, such as horizontal momentum or chemical constituents. The last steps would involve computing fluxes of these quantities; however, explicit formulations for these fluxes are left to future work.

3 Comparison with LES

3.1 LES configuration

We will evaluate the MAP by comparing its characteristics with deep convection in the LES of Peters, Nowotarski, and Mullendore (2020). These simulations use Cloud Model 1 version 18 (CM1, Bryan & Fritsch, 2002) with domain dimensions of 100 by 100 km by 22 km in the x, y, and z directions respectively, and an isotropic 100 m grid spacing. Microphysical processes were parameterized using the double moment microphysics scheme of Morrison et al. (2009) with hail as the prognostic rimed ice species. Convec-

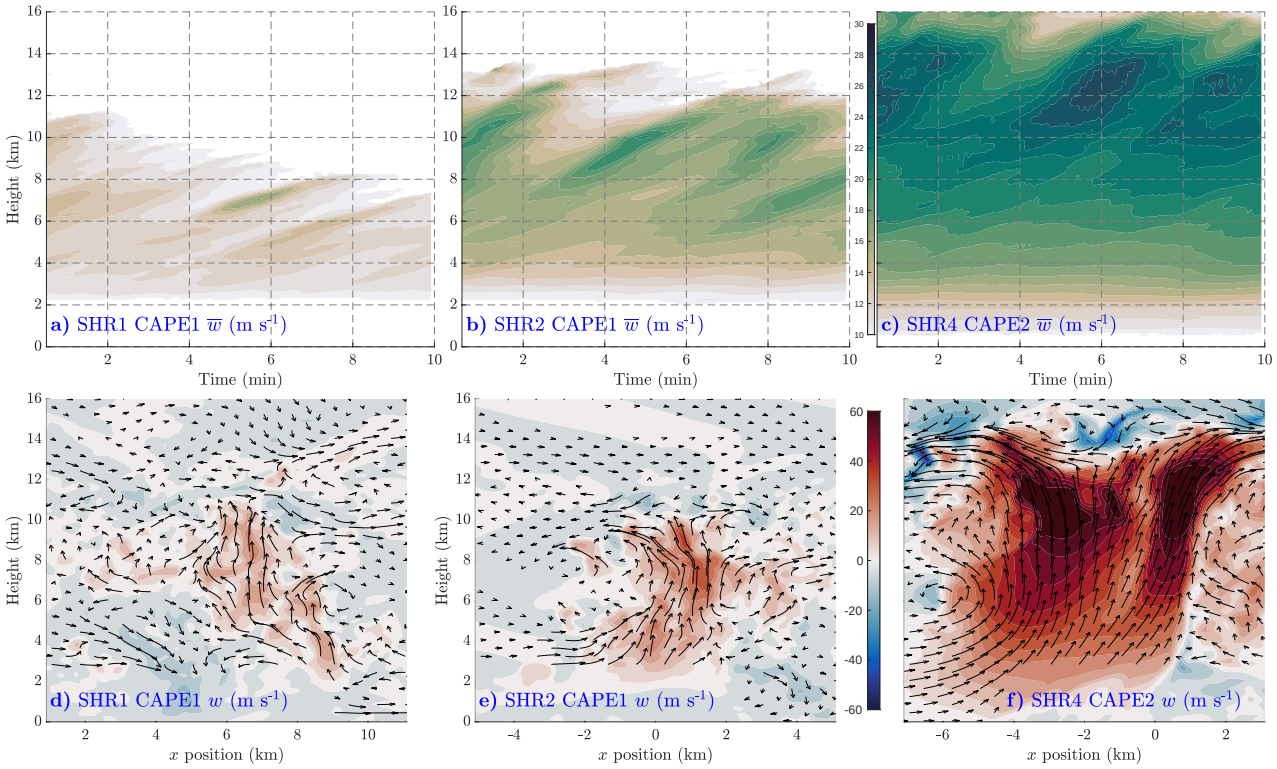

Figure 1. Panels a-c: time (x axis, min) vs height (y axis, km) diagrams of w averaged over the region of $>$ 10 m s^{-1} updraft (shading). Panels d-f: instantaneous snapshots of w (shading, m s^{-1}) and streamlines (black arrows). The left panels show the SHR1 CAPE1 run, the middle panels show the SHR2 CAPE1 run, and the right panels show the SHR4 CAPE2 run. Panels d and e are valid at 1 hour, and panel f is valid at 3 hours.

tion was initiated with a warm bubble, and random noise was included in the initial conditions to facilitate the development of turbulence. For simplicity, large scale tendencies were not imposed in these simulations, and the lateral boundaries were continuously fed the initial model sounding. We therefore focus our comparisons on normalized profiles of quantities from the CPs with analogous normalized profiles from the model because there are no large scale tendencies to provide closure for the CPs. We used two different configurations of the analytic sounding of Weisman and Klemp (1982) with boundary layer mixing ratio values of 14 and 16 g kg^{-1}, which gave two different CAPE values (hereafter CAPE1 and CAPE2), and a constant relative humidity (RH) of 45 % above 3 km as initial thermodynamic profiles (for a skew-T diagram of this profile, see Fig. 1a in Peters, Nowotarski, & Mullendore, 2020). Three different initial wind profiles were used with linear vertical wind shear, and bulk wind differences of 12.5, 25, and 37.5 m s^{-1} respectively (hereafter SHR2, SHR3, and SHR4) over the lowest 6 km, and constant u wind above 6 km (for a graphical representation of this wind profile, see Fig. 1b in Peters, Nowotarski, & Mullendore, 2020). To expand the range of vertical wind shear conditions evaluated here, we generated two new runs with the exact same configuration as the others, but with a 0-6 km bulk wind difference of 6.25 m s^{-1} (hereafter SHR1). These two boundary layer mixing ratio values and four different wind profiles resulted in 8 different simulations — each with its own unique initial model profile. As a first order test of the response in LES behavior to variations in environmental RH, we re-ran the SHR1 CAPE1 and SHR1 CAPE2 runs with the middle tropospheric RH set to 0.85, rather than 0.45 in the original runs.

Simulations were run for 3 hours, with model data output every 5 minutes. Very high temporal resolution output was required for the entrainment calculations that will be discussed shortly. We therefore re-ran 10 minutes of each simulation (starting from restart files) and output model variables every 5 seconds during this 10 minute period for budget calculations. Because of differences in the time periods when deep convection achieved its maximum intensity among simulations, these 10 minute re-runs occurred at 1 hour in the SHR1 and SHR2 runs, and at 3 hours in the SHR3 and SHR4 runs. Additional details of these model runs and high temporal resolution re-runs are available in Peters, Nowotarski, and Mullendore (2020).

As discussed in detail in Peters, Nowotarski, and Mullendore (2020), the character of the convection in these simulations was strongly modulated by the magnitude of the vertical wind shear. Persistent clusters of thermal-like deep convection occurred in the SHR1 and SHR2 runs (Fig. 1a-b, d-e). In contrast, the SHR4 runs produced comparatively steady and wide plume-like updrafts through most of the troposphere (Fig. 1c,f).

Updraft cores were defined as any grid point with $w > 1$ m s^{-1} and $q_c + q_i > 1 \times 10^{-2}$ g kg^{-1} (where q_c and q_i are the cloud water and cloud ice mixing ratios respectively). The method outlined by Romps (2010) was used to compute the budget terms related to ε and δ. In this calculation, $D \equiv \left\langle \max\left(-\frac{d\rho\sigma}{dt}, 0\right)\right\rangle$ and the detrained properties of an arbitrary scalar Λ_D were computed as $\Lambda_D \equiv \frac{\left\langle \max\left(-\frac{d\rho\sigma}{dt},0\right)\Lambda\right\rangle}{\left\langle \max\left(-\frac{d\rho\sigma}{dt},0\right)\right\rangle}$. In these equations σ is set to 0 outside the updraft and 1 inside the updraft, and $<>$ is a horizontal integral over the domain.

An additional sounding from a moist, marine tropical environment was derived from rawinsonde data collected during the Atmospheric Radiation Measurement (ARM) Madden-Julian Oscillation Investigation Experiment (AMIE; Yoneyama et al. (2013)) and is shown in Fig. 2a. Rawinsonde data were post-processed and quality controlled according to Ciesielski et al. (2014). Temperature and horizontal wind were represented by mean values across all soundings collected between 1 October 2011 and 15 January 2012. The specific humidity profile was the mean value observed during times when radar-derived rainfall within an approximate 150 km radius of the rawinsonde launch site was in the upper quartile

of all rain rates observed during the same time period. Surface pressure and humidity were those observed during the rainy periods, and surface temperature was the mean across all available soundings.

The AMIE sounding was used to initialize another CM1 run, with the following specifications that were different from the others . The horizontal grid spacing was set to 100 m, and the vertical grid spacing was set to 50 m in the lowest 2 km, linearly stretched to 250 m in the 2-3.5 km layer, and was held constant at 250 m up to 20 km (the model top). East and west domain dimensions were 64 by 64 km, and east and west boundary conditions were set to periodic. Surface fluxes were turned on to correspond to a fixed sea surface temperature of 305 K. Turbulence was once again seeded with random initial temperature perturbations with an initial amplitude of 0.25 K. The simulation was run for 36 hours, with the horizontally averaged model state evolving toward the profile depicted in Fig. 2b from roughly 15 hours onward. The first 20 hours of the simulation were characterized by scattered shallow-to-mid level convection with maximum cloud top below 10 km. Beyond 20 hours (e.g., Fig. 2c-d), intermittent transient bursts of deep convection (i.e., cloud tops up to 18 km) occurred, and were interspersed with less active periods where predominantly shallow convection resumed. Updrafts were defined in an identical manner in this simulation as they were in the other simulations.

Our investigation of the AMIE simulation served a three-fold purpose:

- It demonstrates the MAP performance in a tropical environment, which contrasts with the soundings used in the other simulations which are more characteristic of continental convection;
- It allows us to evaluate our choice of 1500 m for a lower bound on R_m;
- It allows us to evaluate the performance of the MAP in emulating long term (i.e. several hour) temporal means of M in deep convective environments (recall that we are only evaluating 10 minute periods in the other simulations). Because calculations from the AMIE run are performed over several hour periods of time, we only compare MAP predicted M with AMIE LES M, because outputting at the temporal frequency (i.e., every 5 seconds) necessary to perform detrainment calculations was unfeasible for such a long model integration.

3.2 Comparisons between the updraft core model and LES

To evaluate the MAP, we need to address a few important questions:

- How does the MAP M distribution compare with the traditional plume M formulation in the ZM scheme?
- How reasonable are our assumptions about the initial cloud size distribution?
- How does the MAP respond to variations in the slope constant χ used to define the initial updraft distribution?
- Does the MAP reasonably replicate LES vertical profiles of the quantities discussed in previous sections?
- How does the MAP respond to variations in background RH?
- How does the performance of the MAP depend on the number of radius bins used in our updraft size distribution?

How does the MAP M distribution compare with the traditional plume M formulation in the ZM scheme?

To provide a benchmark for the behavior of the MAP, we compare the distributions of dM, E, and D from the MAP with those of the ZM scheme. The ensemble of clouds in the ZM scheme is determined by assuming that a separate cloud reaches its LNB at each grid point between the level of minimum tropospheric h^*, and the height

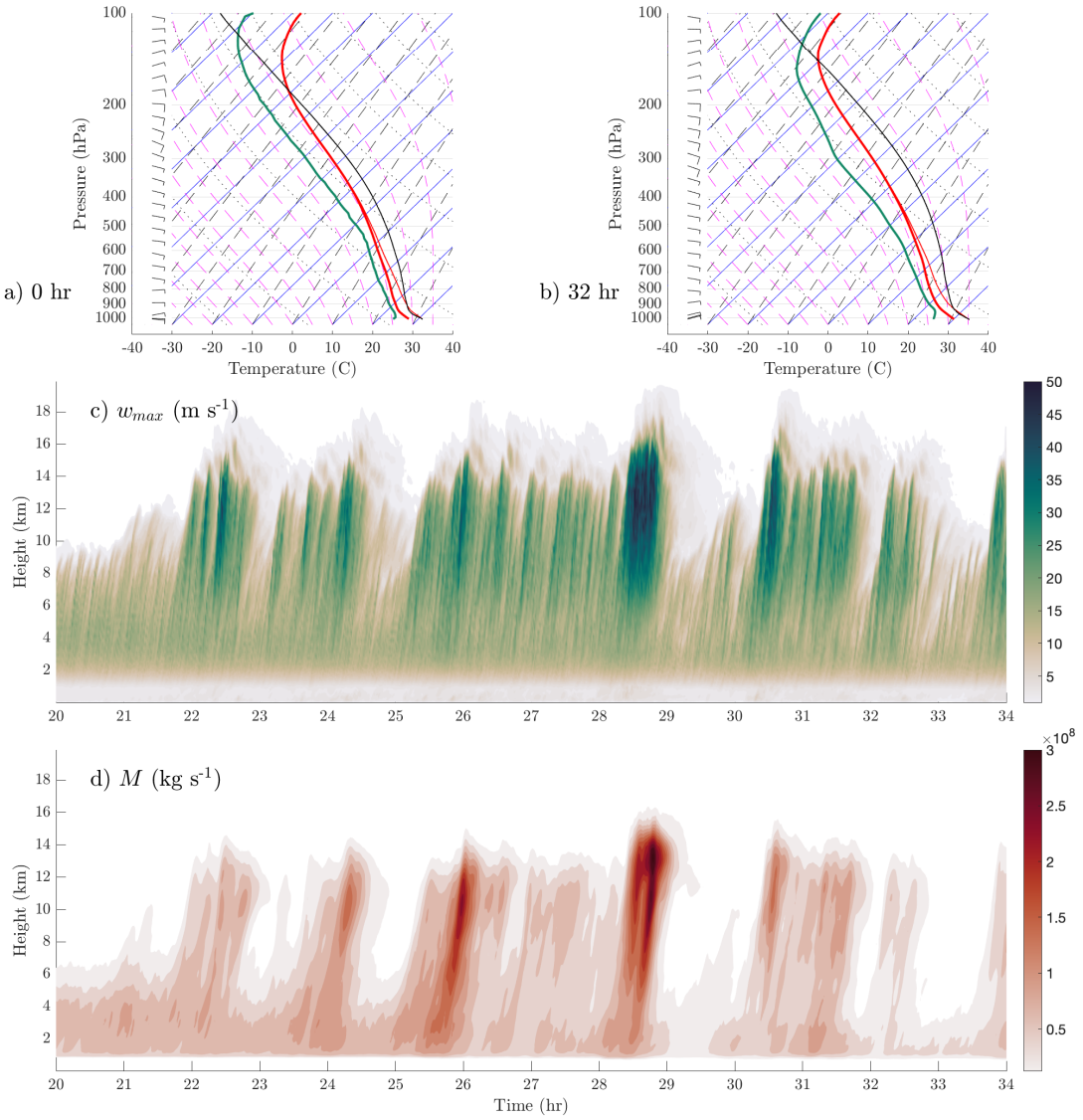

Figure 2. Panels a-b: skew-T log P diagrams showing temperature (thick red, K), dew point temperature (thick green, K), virtual temperature (thin red, K), and the lifted parcel temperature (black, K) for an air parcel with the average properties of the lowest 1 km of the atmosphere. Panel a: the initial sounding in the AMIE simulation. Panel b: sounding characterizing the horizontally averaged state in the AMIE simulation after 32 hours of model integration. Panel c: time-height diagram of maximum w (shading, m s^{-1}) at each vertical level. Panel e: time-height diagram of M (shading, kg s^{-1}) for convective updrafts.

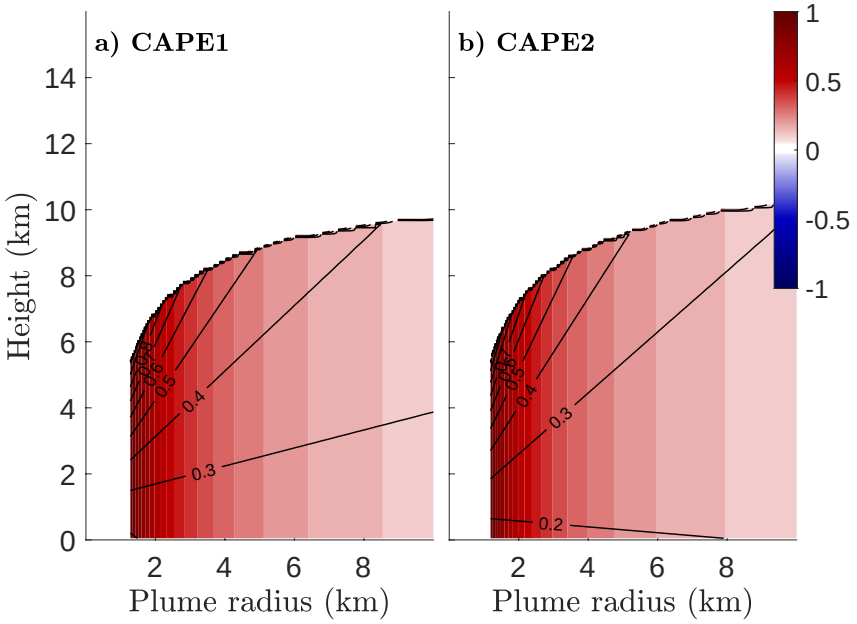

Figure 3. $\frac{dM}{\max(dM)}$ (i.e., dM calculated from eq. 10) from the ZM scheme for the two different CAPE values (panel a, CAPE1; panel b: CAPE2) used among our simulations (black contours), and $\frac{\frac{\partial}{\partial z}dM}{\max(\frac{\partial}{\partial z}dM)}$ (shading). Blue colors (corresponding to detrainment) do not appear because detrainment only occurs within a narrow range at the top of each plume.

of the equilibrium level for an undiluted parcel lifted from the height of maximum h in the lower troposphere. Once this range of LNB heights among the cloud population is established, a numerical procedure calculates the individual entrainment rate for each plume that would have been needed for that plume to reach its respective LNB height, with larger fractional entrainment values corresponding to lower LNBs and smaller entrainment values corresponding to higher LNBs. Thus, the cloud ensemble in the ZM scheme is determined by a range of entrainment rates, rather than cloud widths as is done in the MAP. We may, however, use the analytic formula $\varepsilon = \frac{2k^2}{P_r R}$ for turbulent entrainment from Morrison (2017) to convert an entrainment rate into an associated cloud radius ($R = \frac{2k^2}{P_r \varepsilon}$), so that we can make an apples-to-apples comparison between the ZM scheme and the MAP. For convenience, all quantities used in comparisons between the ZM scheme and MAP are divided by their maximum values among the entire cloud ensemble.

The unphysical behavior of the traditional plume formulation in the ZM scheme is immediately apparent in Fig. 3. The smallest plumes with the largest entrainment rates carry the largest percentage of the M. Furthermore, the maximum M is confined to the upper reaches of the smallest clouds, rather than in the middle troposphere well below cloud top height where it should be. Finally, detrainment does not even show up in the plots because it only occurs within a very narrow layer at cloud top.

The MAP shows markedly different M behavior than the traditional plume approximation (Fig. 4). Peaks in dM occur in the middle troposphere, and at R of 0.5 km in the weakly sheared runs to 0.75-1.5 km in the strongly sheared runs. In other words, the MAP suggests that the peak in M should occur within updrafts of intermediary sizes, rather than the smallest updrafts. This is actually quite consistent with LES, which generally show peaks in M with thermals of R in the 0.5 to 1.5 km range (e.g., Sherwood et al., 2013; Romps & Charn, 2015; Hernandez-Deckers & Sherwood, 2016; Peters, Han-

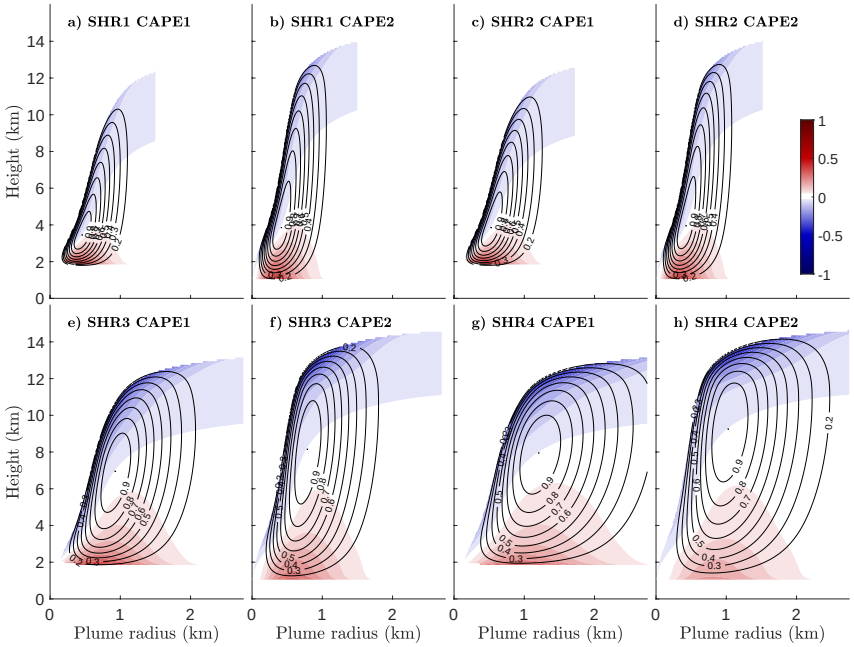

Figure 4. $\frac{dM}{\max(dM)}$ (black contours) for MAP plume radii ranging from $R_0(z)$ to R, and the relative magnitude of $\frac{\frac{\partial}{\partial z}dM}{\max(\frac{\partial}{\partial z}dM)}$ (shading, with red indicating net entrainment and blue indicating net detrainment). Each panel corresponds to the run listed in the upper-left corner.

nah, & Morrison, 2019). Another stark difference between the MAP and the traditional plume formulation is that peak M typically occurs well below cloud top, which is consistent with the behavior of real convection.

It should be noted that the partitioning of the largest percentage of M toward the most dilute clouds only pertains to the ZM scheme because due to its assumption that the cloud base M is identical among all cloud sizes. Other ensemble schemes employ different closure methods for cloud base M (e.g., Arakawa & Schubert, 1974; Moorthi & Suarez, 1992; Chikira & Sugiyama, 2010), and the M profile comparison between the MAP and other schemes may vary substantially from what is portrayed here.

How reasonable are our assumptions about the initial cloud size distribution?

As a rudimentary check of our assumed size distribution of updrafts, we quantified the updraft sizes in LES by first computing the vertical maxima in w within the 3-7 km layer, and then identifying contiguous areas of $w > 1$ m s^{-1} in the 3-7 km max w field. The 3-7 km layer was used for this analysis because it was sufficiently high to avoid regions of lifting along cold pool edges, and sufficiently low to avoid ascent within cumulonimbus anvils and within gravity waves propagating along the tropopause. The distributions of LES updrafts are compared to the MAP distribution in the parameter space of R and $\ln \frac{dN}{dR}$, where $\frac{dN}{dR}$ is computed from LES by binning updraft effective radii $R \equiv \sqrt{\frac{A}{\pi}}$ (where A is the updraft area) at intervals of 100 m. LES distributions generally follow a constant slope for smaller updrafts and level off for larger sizes. In a qualitatively consistent manner with our assumed updraft size distributions, the LES slopes generally increased as shear decreased, though the slopes in the simulations were somewhat steeper than those used in the MAP model (Fig. 5). These differences in slope steepness are likely to be substantially sensitive to the method used for measuring updraft

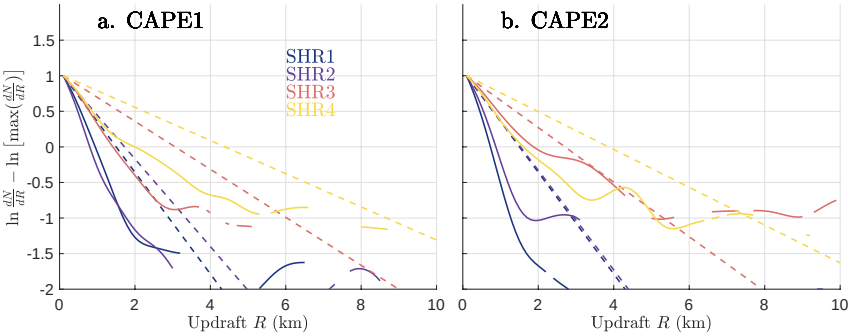

Figure 5. Profiles of the ln of $\frac{dN}{dR}$, normalized by the maximum, from the 3-7 km updrafts identified in LES (solid curves) vs the assumed profiles in the MAP (dashed lines). Panel a: the CAPE1 runs, and panel b: the CAPE2 runs. Colors correspond to different initial shear profiles, as indicated in panel a.

R in the simulations, so we will not quibble over the exact overlap between the dashed and solid lines in fig. 5.

How does the MAP respond to variations in the slope constant χ used to define the initial updraft distribution?

For simplicity, $M(R_m, z)$ (i.e., the total vertical ensemble mass flux) will be simply referred to as M henceforth. We begin our analysis of the MAP performance by evaluating the sensitivity of the MAP M and D profiles to variations in χ. We normalized these profiles with the vertical integrals of M and D so that the area between each M and D profile and the y axis was equal to 1. For our sensitivity tests, and to determine the optimal value for χ, we evaluated profiles of M and D with values of χ ranging from 5 through 14.

The behavior of M profiles are shown in Fig. 6. All of the curves fall within a reasonable distance of the LES M profile. In general, large values of χ correspond to a downward shift in the M profiles among the runs relative to small values of χ - particularly in the case of the runs with small vertical wind shear magnitudes (i.e., Fig. 6a-d). This behavior is somewhat intuitive, given that larger χ shifts more updrafts toward the narrow end of the updraft size distribution, relative to smaller χ. Consistent with this result, large values of χ also correspond to a downward shift in the D profile relative to small values of χ (i.e., Fig. 7).

The root-mean square error (RMSE) was computed for the M and D profiles between the MAP and LES results to evaluate the performance of our choices for χ quantitatively. This RMSE value was normalized by the root-mean square of the LES M profile to yield normalized RMSE (referred to as simply "RMSE"). Minima in RMSE for M among runs were generally in the 9 to 12 range for χ, with the average minima occurring at $\chi = 10$ (Fig. 8). This is the value of $\chi = 10$ we will use hereafter.

Does the MAP reasonably replicate vertical profiles from LES?

Next, we concentrate on comparisons between the MAP and LES profiles of M and D, using $\chi = 10$ in the MAP. To provide a baseline for this comparison, we also compare normalized M and D profiles from the ZM scheme. Correspondence between the MAP and the LES M profiles is remarkably close (Fig. 9). The LES feature "bottom heavy" M profiles in the SHR1 and SHR2 runs, with maxima of M in the 2-4 km layer, and a gradual decline in M above this level. The MAP faithfully replicates this behav-

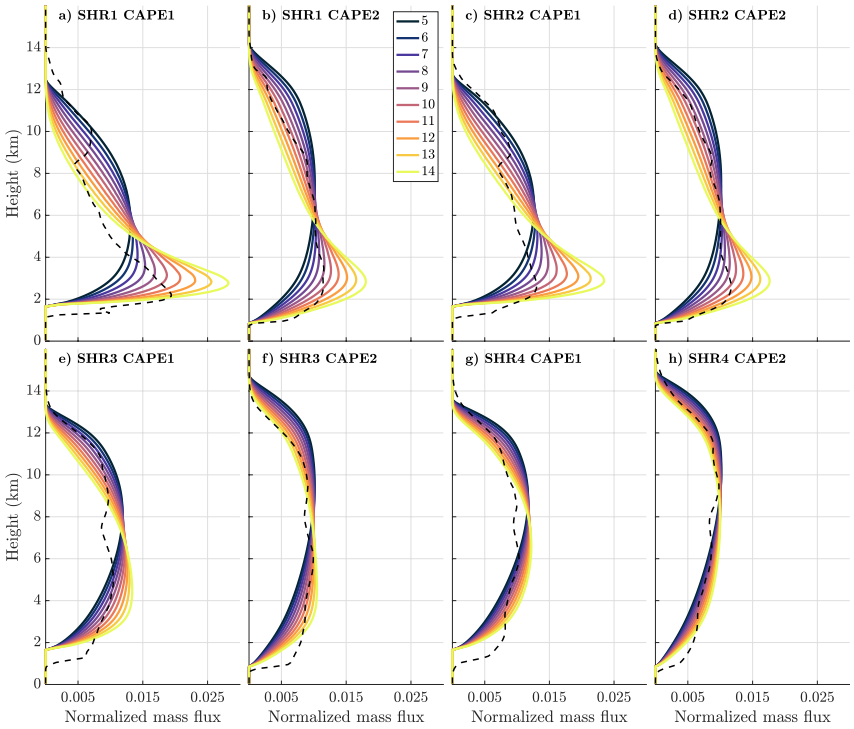

Figure 6. Normalized vertical profiles of M from the MAP (colored lines) and LES (black dashed lines). Each color corresponds to a different χ value, as indicated in the legend in panel b. Each panel corresponds to the run listed in the upper-left corner of that panel.

ior in low shear environments. As the shear increased in the LES runs, the maximum in LES M broadened and transitioned into the middle (i.e., 4-8 km in the SHR3 and SHR4 CAPE1 runs) and upper (i.e., 8-12 km in the SHR4 CAPE2 run) troposphere. Again, a nearly identical behavior is present in the MAP. The MAP M profiles improve substantially upon the ZM profiles — the later of which do not take into account the wind shear differences between the environments. The comparison with the ZM M profile is closest for the LES with the weakest shear; however, the height of maximum M in the ZM scheme is 3-4 km higher than in LES. In the runs with larger shear, the peak in the ZM mass flux is biased toward low-levels when compared to the LES. Average linear correlation coefficients (CC) between MAP and LES M were 0.94, and between ZM and LES M were 0.75.

In the case of the AMIE LES, we concentrated on the time period that was actively producing deep convection, which was between 21 and 34 hours. The vertical wind shear was very weak in this sounding (e.g., less than 5 m s^{-1}, Fig. 2a-b), so R_m was set to 1500 m in accordance with the convention outlined in the previous section. Comparisons of the 21-34 hour averaged M with the MAP show remarkable correspondence (Fig. 10a), with $CC = 0.94$. The performance of MAP is a marked improvement over the ZM scheme, with which $CC = 0.81$. To evaluate the sensitivity of the MAP performance to the choice of the lower bound of R_m, we compared MAP M with choices of R_m ranging from 500 m to 2250 m to the AMIE LES (Fig. 10b). Unsurprisingly, lower values of R_m depict a shallow convective regime with M primarily confined to the lowest few km of the troposphere, whereas larger values of R_m depict a progressively more "top-heavy" M distribution. MAP performance was best with optimized with $R_m = 1500$ m, with a CC of 0.95 (Fig. 10c) which corroborates our usage of this parameter value.

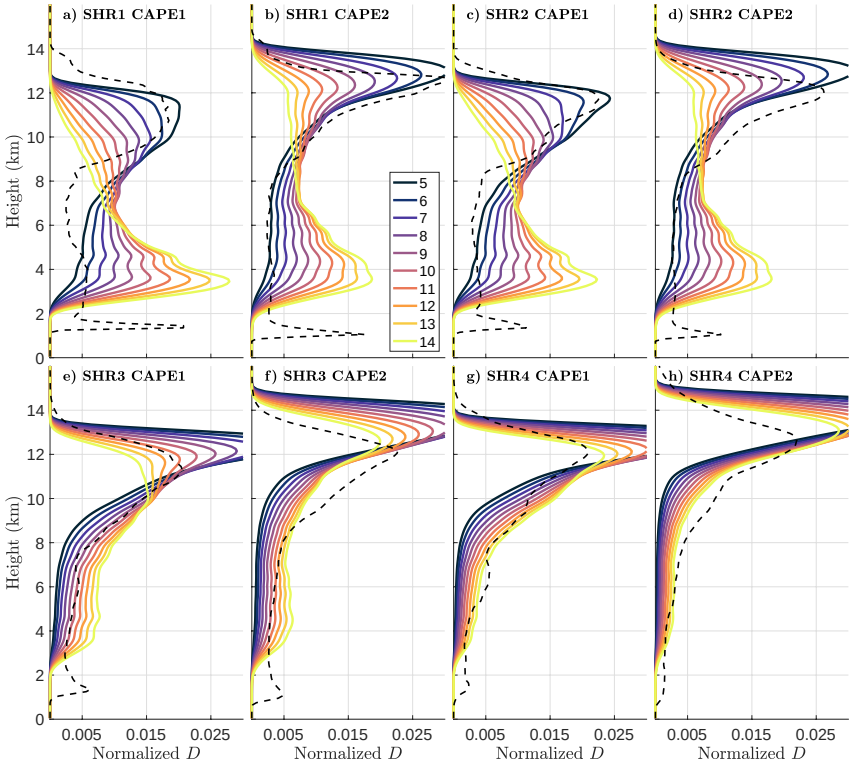

Figure 7. Normalized vertical profiles of D from the MAP (colored lines) and LES (black dashed lines). Each color corresponds to a different χ value, as indicated in the legend in panel b. Each panel corresponds to the run listed in the upper-left corner.

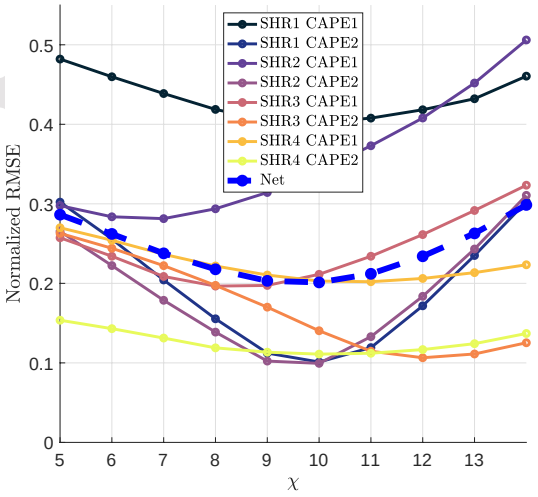

Figure 8. Normalized RMSE (y axis) of the MAP model relative to LES for M as a function of χ (x axis). Each color corresponds to a different LES run, as indicated in the legend.

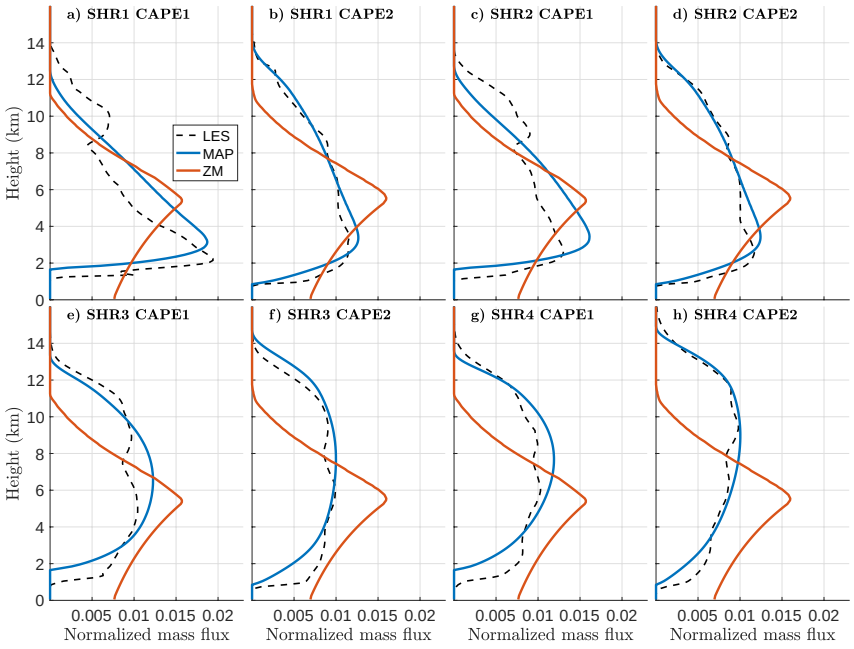

Figure 9. Comparison of the 10 minute temporal average of M from the LES simulations (black dashed line) with MAP M (blue) and the ZM M (red). Each panel corresponds to the run listed in the upper left. Each M curve has been divided by the area under the curve yielding "normalized mass flux" to facilitate comparisons among runs, and between MAP and the LES output.

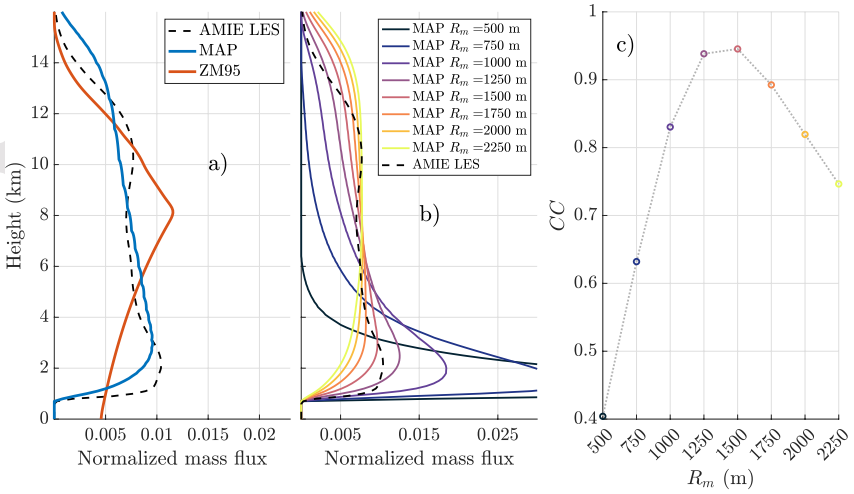

Figure 10. Pane a: as in Fig. 9, but comparing the MAP and ZM with the AMIE LES. Panel b: a comparison of MAP M as a function of choices for the lower bound of R_m that range from 500 m to 2250 m (colors) with AMIE LES (black dashed). Panel c: CC between the MAP and AMIE LES as a function of choices for the lower bound of R_m that range from 500 m to 2250 m.

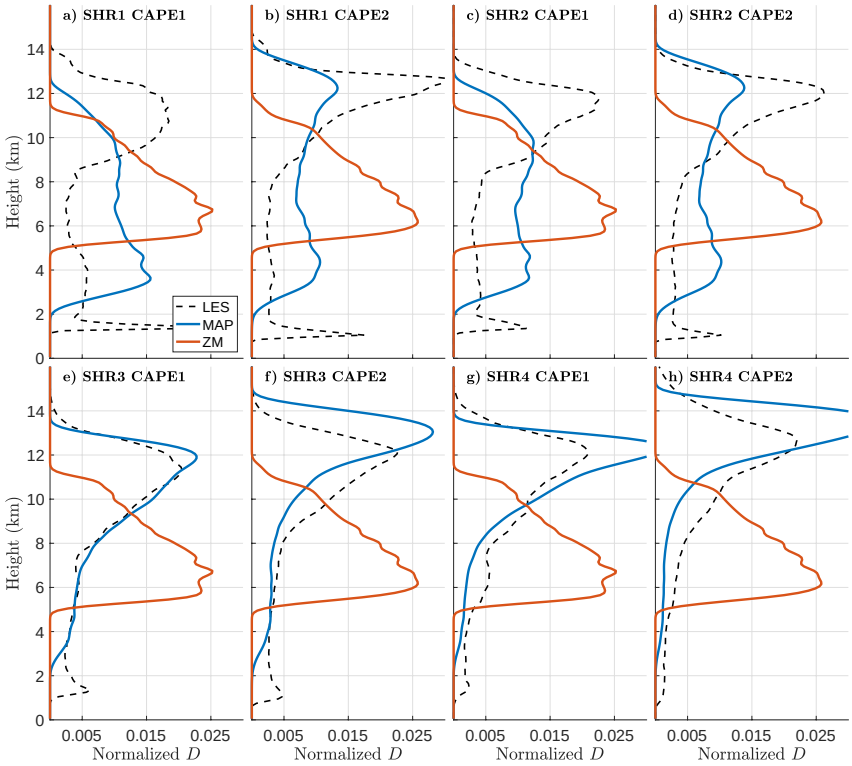

Figure 11. Comparison of the 10 minute temporal average of D from the LES simulations (black dashed line) with MAP D. Each panel corresponds to the run listed in the upper left. Each D curve has been divided by the area under the curve yielding "normalized detrainment" to facilitate comparisons among runs, and between MAP and the LES output.

Comparisons between the MAP and LES D profiles (Fig. 11) are somewhat less favorable in the SHR1 and SHR2 runs, with the MAP showing a maximum in D at an unrealistically low height compared to the LES. This problem becomes gradually less pronounced as shear increased, with the comparison between MAP and LES D greatly improved in the SHR3 and SHR4 runs. There are, however, several realistic attributes of the MAP D that are present among all runs. The LES show detrainment occurring through most of the depth of the troposphere, which is also portrayed in the MAP. In contrast, D in the ZM model is unrealistically confined to a 5-12 km layer among all runs. Thus, despite some inconsistencies between the MAP and LES at low shear values, the MAP improves the prediction of D in all simulations over the ZM scheme. Average CC between MAP and LES D were 0.72, and between ZM and LES M were 0.13.

Finally, we must evaluate assumptions about the properties of detrained air in the MAP. A comparison between h_D computed from LES and h^* computed using the initial model profiles shows close correspondence between these variables (Fig. 12), suggesting that our approximation that $h_D = h^*$ is a reasonable one. Furthermore, the qualitative behavior of detrained cloud water and ice portrayed by the MAP is consistent with the detrainment of parameterized microphysical variables in the LES (Fig. 13). Quantitative comparisons for the detrained microphysical variables are reasonable as well, aside from a low bias in the MAP ice detrainment aloft of 25-50%. Average CC between MAP and LES liquid and ice were a respectable 0.84 and 0.93 respectively. We do not directly compare the MAP with the ZM scheme here because the ZM scheme is often coupled

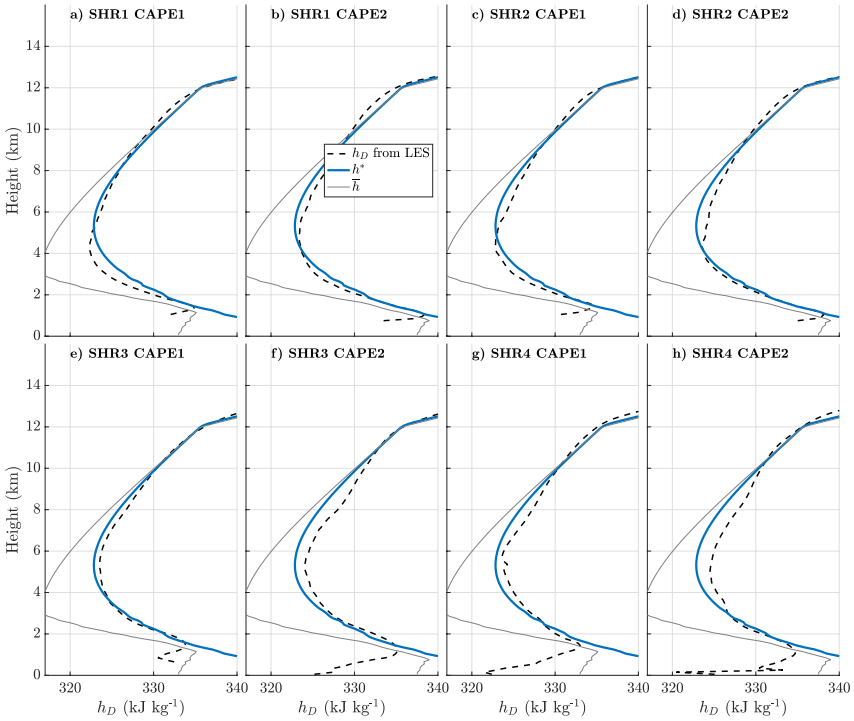

Figure 12. A comparison of vertical profiles of h^* (kJ kg^{-1}, blue lines), h_D computed from LES (kJ kg^{-1}, dashed black lines), and $\overline{h}$ from simulations (kJ kg^{-1}, thin gray line). Each panel corresponds to the run listed in the upper-left corner.

with comparatively sophisticated microphysics, meaning that the comparison is not apples-to-apples.

How does the MAP respond to variations in background RH?

It is well known that the deleterious effects of entrainment-driven dilution on updraft B are strongly sensitive to the RH of the background environment (e.g., Morrison, 2017; Morrison et al., 2020; Peters, Morrison, Hannah, et al., 2020). To this end, existing parameterizations have incorporated ad hoc parameters that modify fractional entrainment rates as a response to evolving environmental RH (e.g., Mapes & Neale, 2011), or have even gone so far as to formulate entrainment rates to be directly dependent on environmental moisture (e.g., Bechtold et al., 2008; Han et al., 2017). It was further noted by Peters, Nowotarski, and Morrison (2019) that the differences in entrainment-driven dilution in low RH and high RH environments was more pronounced when vertical wind shear was weak and updrafts were narrow, than when vertical wind shear was strong and updrafts were wide. Ideally, the MAP would replicate this behavior in that M profiles should be more sensitive to environmental RH when shear is weak, than when shear is strong.

The increase in RH to 0.85 in the RH sensitivity runs resulted in an upward shift in the M distribution, as a response to reduced entrainment-driven dilution of core B relative to the 0.45 RH runs (Fig. 14a-b). When subject to background RH ranging from 0.1 to 1.0, the MAP emulates the aforementioned behavior. In addition, the MAP shows a diminished dependence of updraft core dilution on RH when shear is strong, updrafts are wide, and fractional entrainment rates are minimal, which is consistent with the results of Peters, Nowotarski, and Morrison (2019). In low RH environments, M is displaced substantially downward in the weakly sheared environments because of a shallowing of

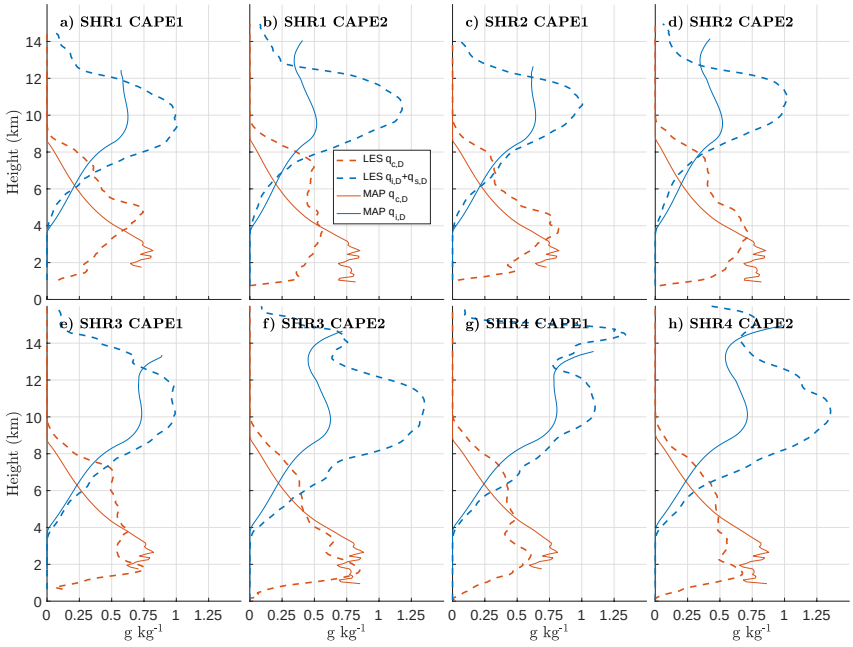

Figure 13. A comparison of vertical profiles of detrained cloud water from the Morrison and Gettelman (2008) microphysics scheme ($q_{c,D}$, g kg^{-1}, red dashed line), detrained cloud ice plus snow from the Morrison and Gettelman (2008) microphysics scheme ($q_{i,D} + q_{s,D}$, g kg^{-1}, blue dashed line), cloud water from the MAP (g kg^{-1}, red solid line), and cloud ice from the MAP (g kg^{-1}, blue solid line). Each panel corresponds to the run listed in the upper-left corner.

the cloud population (Fig. 14a-d). This contrasts with high RH environments, wherein M is displaced substantially upward because of a comparative deepening of the cloud population (Fig. 14e-h). This sensitivity was substantially subdued in the higher shear runs, consistent with the results of Peters, Nowotarski, and Morrison (2019).

How does the performance of the MAP depend on the number of radius bins used in our updraft size distribution?

It is generally desirable for a CP to require minimal computational resources, so it minimally affects the speed of integration of the parent GCM. As a last check on the performance of our model, we evaluate the sensitivity of M profiles to the radius bin size ΔR used to discretize the initial cloud size distribution for numerical integration. For all figures shown thus far, we have used $\Delta R = 10$ m. Here, we evaluate ΔR ranging from 1 m all the way to 500 m. While curves for all ΔR generally center around the LES curve, there is considerably more artificial noise in the M profile for $\Delta R > 100$ m for most runs (Fig. 15) compared to using $\Delta R < 100$ m. There is even subtle noisiness in the vertical profile for $\Delta R = 100$ m in the runs with the weakest shear (Fig. 15a-d). Applying a simple vertical moving average filter to M reduces this noise considerably (not shown), making ΔR as large as 250 m potentially suitable for operational use.

4 Summary and conclusions

In this article, we present an approach for modeling deep convective cores in CPs that builds upon several previous schemes that employ cloud ensembles (Donner, 1993; Wagner & Graf, 2010; Neggers, 2015). In this model (which we call the MAP, for "multiplume analytic model"), properties of clouds are represented through an ensemble of up-

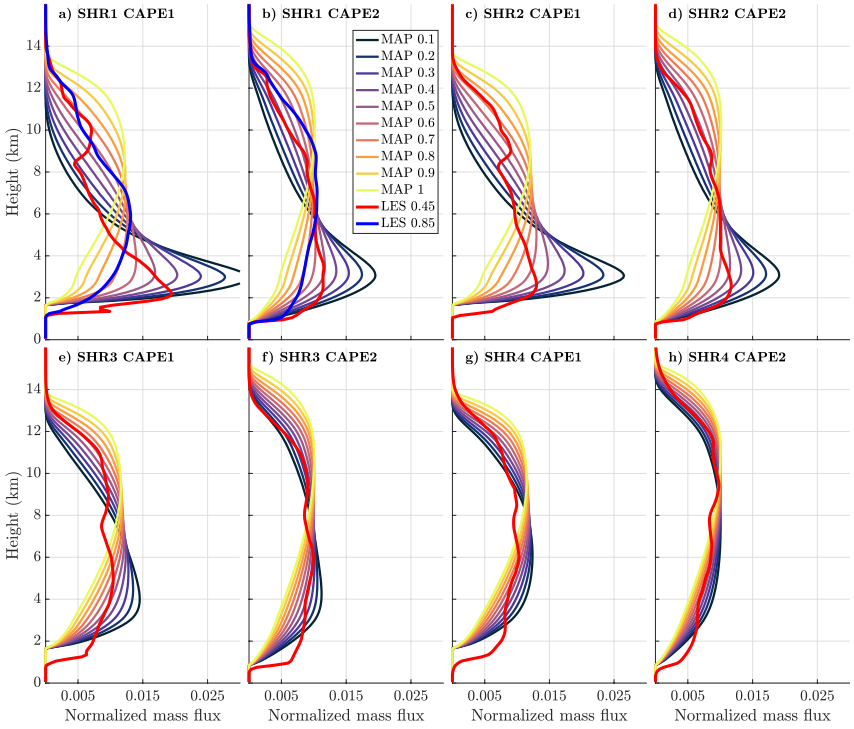

Figure 14. Normalized profiles of M from the MAP (colored lines) and LES ($RH = 0.45$, red, $RH = 0.85$, blue). Each color corresponds to a different RH value. Each panel corresponds to the run listed in the upper-left corner.

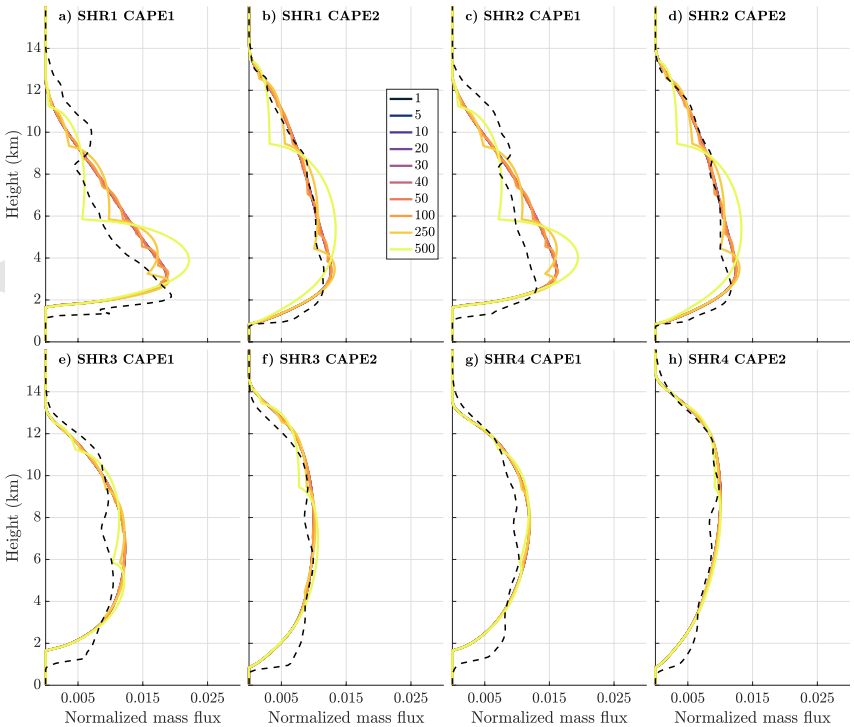

Figure 15. Comparisons of MAP M (colors) with LES (black dashed) as a function of the bin size (m, legend in panel b) used to discretize the updraft size distribution.

drafts with R determined from a specific size distribution, and fractional entrainment rates are formulated with an inverse relationship with cloud radius. We assume updraft radii are constant with height and predict M using analytic equations for buoyancy and vertical velocity. The MAP also incorporates the influences of vertical wind shear on the properties of the cloud ensemble, allowing for a greater number of wider updrafts when vertical wind shear is large, compared to when vertical wind shear is small. The MAP is formulated to work with existing cloud base M closure assumptions.

The MAP is evaluated by comparing it with LES that were initialized with varying wind shear and CAPE. Noteworthy results from this comparison are as follows:

- the MAP produces comparable profiles to LES of M, detrainment, and the properties of detrained air;
- optimal values of the free parameters used to initialize the MAP yield M and D profiles that show substantially improved correspondence with LES compared to the ZM scheme;
- increasing vertical wind shear in the LES results in a progression from a bottom-heavy to a top-heavy profile of M. The MAP emulates this behavior.

It is worthwhile to discuss some of the advantages and disadvantages of using a cloud core model akin to the MAP over other parameterization schemes. Advantages are as follows:

- The MAP shows promise in its ability to incorporate the influences of vertical wind shear on cloud behavior. To our knowledge, no other parameterizations connect shear to cloud behavior.
- The MAP predicts entrainment rates, cloud buoyancy, and cloud vertical velocity from analytic formulae with a sound physical basis. In contrast, other parameterization schemes often involve ad-hoc assumptions that lack a physical basis.
- Because many equations are analytic, MAP calls will be comparable to or less computational expensive than other multi-plume schemes.
- Over the limited range of cases studied here, the MAP seems to portray cloud properties more accurately than the ZM scheme. Obviously more evaluation of the MAP behavior against LES in different environments and against observations is needed to determine whether this result applies more generally than the situations analyzed here.
- Like in the ED(MF)$^{\mathrm{n}}$ approach, the MAP has potential use as both a shallow and deep CPs, as it makes no parametric assumptions that are specific to either shallow or deep convection.
- Like in the ED(MF)$^{\mathrm{n}}$ approach, the MAP is formulated for scale awareness because the vertical profile of fractional cloud area is explicitly predicted by the set of equations.
- Our closure configuration for the MAP is left open-ended. Though we have paved the way for using existing closure schemes with this model, it is conceivable that new closure assumptions, such as those that make explicit assumptions about updraft structure below cloud base (e.g., Romps, 2016; Neggers, 2015), could also be used.
- Our strategy for incorporating vertical wind shear could conceivably be applied to another scheme that determines cloud ensemble properties from an assumed distribution of cloud radii, such as the ED(MF)$^{\mathrm{n}}$ scheme.

Disadvantages are as follows:

- The MAP features a larger number of tunable parameters than other parameterizations such as the R and ZM models (though the number here are comparable

to that of the ED(MF)^n approach). Consequently, tuning the model may involve a more extensive array of tests than in other models.

- The MAP will be more computationally expensive than bulk schemes that feature a single plume, or multi-plume schemes where integrations over the range of plumes are accomplished analytically (as in the ZM scheme).

There are some obvious avenues for future work laid out by our list of advantages and disadvantages. The gold standard for evaluating the performance of CPs involves comparisons of CP performance with observations. Such an evaluation needs to be performed in the future. We also need to compare this model's performance to LES in a wider range of environments. This range of environments with realistic radiation and large scale tendencies cloud resolving models with heterogeneity in the initial and lateral boundary conditions (i.e., real-data Weather Research and Forecasting model runs). Another round of tests will compare the MAP large scale tendencies with those in regional simulations by cloud resolving models in both strongly and weakly sheared environments. We have not considered downdrafts or a convective trigger function here because existing formulations for these processes in the ZM scheme can be used in combination with the MAP. However, we plan to investigate avenues for improving the physicality of these these processes in future studies. Finally, we need to evaluate the MAP in a GCM, starting with single column tests, and leading to global runs involving targeted analyses of the GCM's ability to replicate observed large scale atmospheric dynamics.

Acknowledgments

Thanks to Jake Mulholland, Yang Tian, and Roel Neggers for helpful comments and feedback. J. Peters's efforts were supported by the National Science Foundation (NSF) grants AGS-1928666, AGS-1841674, and Department of Energy Atmospheric System Research (DOE ASR) grant DE-SC0000246356. H. Morrison and G. Zhang were supported by DOE ASR grant DE-SC0020104. All scripts used to post-process model data, along with the CM1 namelist for the AMIE simulation, are available via Figshare at `https://figshare.com/articles/software/Data_for_JAMES_publication/13093268`. All other LES model data was used from Peters, Nowotarski, and Mullendore (2020). The source code for CM1 is publicly available at `http://www2.mmm.ucar.edu/people/bryan/cm1/`

References

Arakawa, A., & Jung, J. H. (2011). Multiscale modeling of the moist-convective atmosphere - A review. *Atmos. Res.*, *102*, 263-285.

Arakawa, A., Jung, J. H., & Wu, C. M. (2011). Toward unification of the multiscale modeling of the atmosphere. *Atmos. Chem. Phys.*, *11*, 3731-3742.

Arakawa, A., & Schubert, W. H. (1974). Interaction of a Cumulus Cloud Ensemble with the Large-Scale Environment, Part I. *J. Atmos. Sci.*, *31*, 674-701.

Arakawa, A., & Wu, C.-M. (2013). A unified representation of deep moist convection in numerical modeling of the atmosphere. Part I. *J. Atmos. Sci.*, *70*, 1977-1992.

Bechtold, P., Kohler, M., Jung, T., Doblas-Reyes, F., Leutbecher, M., Rodwell, M. J., ... Balsamo, G. (2008). Advances in simulationg atmospheric variability with the ECMWF model: from synoptic to decadal timescales. *Quart. J. Roy. Meteor. Soc.*, *134*, 1337-1351.

Brown, M., & Nowotarski, C. J. (2018). The influence of lifting condensatioon level on low-level outflow and rotation in simulated supercell thunderstorms. *J. Atmos. Sci.*, *In Review*.

Bryan, G. H., & Fritsch, J. M. (2002). A benchmark simulation for moist nonhydrostatic numerical models. *Mon. Wea. Rev.*, *130*, 2917-2928.

Bryan, G. H., & Rotunno, R. (2014). The optimal state for gravity currents in shear.

J. Atmos. Sci., *71*, 448-468.

Chikira, M., & Sugiyama, M. (2010). A Cumulus Parameterization with State-Dependent Entrainment Rate. Part I: Description and Sensitivity to Temperature and Humidity Profiles. *Journal of the Atmospheric Sciences*, *67*(7), 2171-2193.

Ciesielski, P. E., Yu, H., Johnson, R. H., Yoneyama, K., Katsumata, M., Long, C. N., ... Van Hove, T. (2014, 04). Quality-Controlled Upper-Air Sounding Dataset for DYNAMO/CINDY/AMIE: Development and Corrections. *Journal of Atmospheric and Oceanic Technology*, *31*(4), 741-764. Retrieved from `https://doi.org/10.1175/JTECH-D-13-00165.1` doi: 10.1175/JTECH-D-13-00165.1

Dawe, J. T., & Austin, P. H. (2011). Interpolation of LES cloud surfaces for use in direct calculations of entrainment and detrainment. *Mon. Wea. Rev.*, *139*(444-456).

De Rooy, W. C., Bechtold, P., Frolich, K., Hohenegger, C., Jonker, H., Mironov, D., ... Yano, J. I. (2013). Entrainment and detrainment in cumulus convection: an overview. *Quart. J. Roy. Meteor. Soc.*, *139*, 1-19.

Donner, L. J. (1993). A cumulus parameterization including mass fluxes, vertical momentum dynamics, and mesoscale effects. *J. Atmos. Sci.*, *50*, 889-906.

Grell, G. A., & Freitas, S. R. (2014). A scale and aerosol aware stochastic convective parameterization for weather and air quality modeling. *Atmos. Chem. Phys.*, *14*, 5233-5250.

Han, J., Wang, W., Kwon, Y. C., Hong, S., Tallapragada, V., & Yang, F. (2017). Updates to the NCEP GFS cumulus convection schemes with scale and aerosol awareness. *Wea. Forecasting*, *32*, 2005-2017.

Hannah, W. M. (2017). Entrainment vs. Dilution in Tropical Deep Convection. *J. Atmos. Sci.*, *74*, 3725-3747.

Hernandez-Deckers, D., & Sherwood, S. C. (2016). A numerical investigation of cumulus thermals. *J. Atmos. Sci.*, *73*, 4117-4136.

Hernandez-Deckers, D., & Sherwood, S. C. (2018). On the role of entrainment in the fate of cumulus thermals. *J. Atmos. Sci.*, *75*, 3911-3924.

Hirota, N., Takayabu, Y. N., Watanabe, M., Kimoto, & Chikira, M. (2014). Role of convective entrainment in spatial distributions of andtemporal variations in precipitation over tropical oceans. *J. Climate*, *23*, 8707-8723.

Jeevanjee, N., & Romps, D. M. (2015). Effective Buoyancy, Inertial Pressure, and the Mechanical Generation of Boundary Layer Mass Flux by Cold Pools. *J. Atmos. Sci.*, *72*, 3199-3213.

Khairoutdinov, M., Krueger, S. K., Moeng, C.-H., Bogenshultz, P. A., & Randall, D. A. (2009). Large-eddy simulation of deep tropical convection. *J. Adv. Model. Earth Sys.*, *1*, 13pp.

Kyle, T. G., Sand, W. R., & Musil, D. J. (1976). Fitting measurements of thunderstorm updaft properties to model profiles. *Mon. Wea. Rev.*, *104*, 611-617.

Lecoanet, D., & Jeevanjee, N. (2018). Entrainment in resolved, turbulent dry thermals. *Quart. J. Roy. Meteor. Soc.*, *https://arxiv.org/pdf/1804.09326.pdf*.

LeMone, M. A., & Zipser, E. J. (1980). Cumulonimbus vertical velocity events in GATE. part I: Diameter, intensity, and mass flux. *J. Atmos. Sci.*, *37*, 2444-2457.

Mapes, B. E., & Neale, R. (2011). Parameterizing convective organization to escape the entrainment dilemma. *J. Adv. Model. Earth Sys.*, *3*, 20 pp.

Moorthi, S., & Suarez, M. J. (1992). A paramaterization of moist convection for general circulation models. *Mon. Wea. Rev.*, *120*, 978-1002.

Morrison, H. (2016). Impacts of updraft size and dimensionality on the perturbation pressure and vertical velocity in cumulus convection, Part 1: Simple, generalized analytic solutions. *J. Atmos. Sci.*, *73*, 1441-1454.

Morrison, H. (2017). An analytic description of the structure and evolution of growing deep cumulus updrafts. *J. Atmos. Sci.*, *74*, 809-834.

Morrison, H., & Gettelman, A. (2008). A new two-moment bulk stratiform cloud microphysics scheme in the community atmosphere model, version 3 (CAM3). Part 1: description and numerical tests. *J. Climate*, *21*, 3642-3659.

Morrison, H., & Peters, J. M. (2018). Theoretical expressions for the ascent rate of moist convective thermals. *J. Atmos. Sci.*, *75*, 1699-1719.

Morrison, H., Peters, J. M., Hannah, W. M., Varble, A. C., & Giangrande, S. E. (2020). Thermal chains in ascending moist updrafts: Part 1: Theoretical description. *J. Atmos. Sci.*, *https://doi.org/10.1175/JAS-D-19-0243.1*.

Morrison, H., Thompson, G., & Tatarskii, V. (2009). Impact of cloud microphysics on the development of trailing stratiform precipitation in a simulated squall line: comparison of one and two-moment schemes. *Mon. Wea. Rev.*, *137*, 991-1007.

Neggers, R. A. (2015). Exploring binmacrophysics models for moist convective transport and clouds. *J. Adv. Model. Earth Sys.*, *7*, 2079-2104.

Neggers, R. A., Griewank, P. J., & Heus, T. (2019). Power-law scaling in the internal variability of cumulus cloud size distributions due to subsampling and spatial organization. *J. Atmos. Sci.*, *76*, 1489-1503.

Peters, J. M. (2016). The impact of effective buoyancy and dynamic pressure forcing on vertical velocities within 2 dimensional updrafts. *J. Atmos. Sci.*, *73*, 4531-4551.

Peters, J. M., Hannah, W. M., & Morrison, H. (2019). The influence of vertical wind shear on moist thermals. *J. Atmos. Sci.*, *76*, 1645-1659.

Peters, J. M., Morrison, H., Hannah, W. M., Varble, A. C., & Giangrande, S. E. (2020). Thermal chains in ascending moist updrafts: Part 2: Simulations. *J. Atmos. Sci.*, *https://doi.org/10.1175/JAS-D-19-0244.1*.

Peters, J. M., Morrison, H., Nowotarski, C. J., Mulholland, J. P., & Thompson, R. L. (2020). A formula for the maximum vertical velocity in supercell updrafts. *J. Atmos. Sci.*, *https://doi.org/10.1175/JAS-D-20-0103.1*.

Peters, J. M., Nowotarski, C., & Morrison, H. (2019). The role of vertical wind shear in modulating maximum supercell updraft velocities. *J. Atmos. Sci.*, *76*, 3169–3189.

Peters, J. M., Nowotarski, C., & Mullendore, G. (2020). Are supercells resistant to entrainment because of their rotation? *J. Atmos. Sci.*, *77*, 1475-1495.

Peters, J. M., Nowotarski, C. J., & Mulholland, J. P. (2020). The influences of effective inflow layer streamwise vorticity and storm-relative flow on supercell updraft properties. *J. Atmos. Sci.*, *77*, 3033-3057.

Romps, D. M. (2010). A direct measure of entrainment. *J. Atmos. Sci.*, *67*, 1908-1927.

Romps, D. M. (2016). The stocastic parcel model: a deterministic paramaterization of stochastically entraining convection. *J. Adv. Model. Earth Sys.*, *8*(1), 319-344.

Romps, D. M., & Charn, A. B. (2015). Sticky Thermals: Evidence for a Dominant Balance between Buoyancy and Drag in Cloud Updrafts. *J. Atmos. Sci.*, *72*, 2890-2901.

Romps, D. M., & Kuang, Z. (2010). Do undiluted convective plumes exist in the upper troposphere? *J. Atmos. Sci.*, *67*, 468-484.

Sherwood, S. C., Hernandez-Deckers, D., & Colin, M. (2013). Slippery thermals and the cumulus entrainment paradox. *J. Atmos. Sci.*, *70*, 2426-2442.

Squires, P., & Turner, J. S. (1962). An entraining jet model for cumulo-nimbus updrafts. *Tellus*, *14A*, 422-434.

Thompson, R. L., Mead, C. M., & Edwards, R. (2007). Effective Storm-Relative Helicity and Bulk Shear in Supercell Thunderstorm Environments. *Wea. Forecasting*, *22*, 102-115.

Tian, Y., & Kuang, Z. (2016). Dependence of entrainment in shallow cumulus convection on vertical velocity and distance to cloud edge. *Geophysical Research Letters*, *43*(8), 4056-4065.

Wagner, T. M., & Graf, H.-F. (2010). An Ensemble Cumulus Convection Parameterization with Explicit Cloud Treatment. *Journal of the Atmospheric Sciences*, *67*(12), 3854-3869.

Warren, R. A., Richter, H., Ramsay, H. A., Siems, S. T., & Manton, M. J. (2017). Impact of variations in upper-level shear on simulated supercells. *Mon. Wea. Rev.*, *145*, 2659-2681.

Weisman, M. L., & Klemp, J. B. (1982). The Dependence of Numerically Simulated Convective Storms on Vertical Wind Shear and Buoyancy. *Mon. Wea. Rev.*, *110*, 504–520. doi: http://dx.doi.org/10.1175/1520-0493(1982)110⟨0504:TDONSC⟩2.0.CO;2

Yoneyama, K., Zhang, C., & Long, C. N. (2013, 12). Tracking Pulses of the Madden–Julian Oscillation. *Bulletin of the American Meteorological Society*, *94*(12), 1871-1891. Retrieved from `https://doi.org/10.1175/BAMS-D-12-00157.1` doi: 10.1175/BAMS-D-12-00157.1

Zhang, G. J., & McFarlane, N. A. (1995). Sensitivity of climate simulations to the paramaterization of cumulus convection in the Canadian climate center general-circulation model. *Atmosphere-Ocean*, *33*, 407-446.